



Distinct cellular dynamics associated with response to CAR-T therapy for refractory B cell lymphoma

Nicholas J. Haradhvala^{ID 1,2,9}, Mark B. Leick^{3,4,9}, Katie Maurer^{ID 2,5,9}, Satyen H. Gohil^{2,5,6,9}, Rebecca C. Larson^{3,4}, Ning Yao^{2,7}, Kathleen M. E. Gallagher^{3,4}, Katelyn Katsis³, Matthew J. Frigault^{ID 3,4}, Jackson Southard⁵, Shuqiang Li^{2,5}, Michael C. Kann^{ID 3}, Harrison Silva³, Max Jan^{3,4}, Kahn Rhrissorakrai⁸, Filippo Utro^{ID 8}, Chaya Levovitz^{ID 8}, Raquel A. Jacobs², Kara Slowik², Brian P. Danysh^{ID 2}, Kenneth J. Livak^{ID 5}, Laxmi Parida^{ID 8}, Judith Ferry³, Caron Jacobson⁵, Catherine J. Wu^{ID 2,5,10}✉, Gad Getz^{ID 2,3,4,10}✉ and Marcela V. Maus^{ID 2,3,4,10}✉

Chimeric antigen receptor (CAR)-T cell therapy has revolutionized the treatment of hematologic malignancies. Approximately half of patients with refractory large B cell lymphomas achieve durable responses from CD19-targeting CAR-T treatment; however, failure mechanisms are identified in only a fraction of cases. To gain new insights into the basis of clinical response, we performed single-cell transcriptome sequencing of 105 pretreatment and post-treatment peripheral blood mononuclear cell samples, and infusion products collected from 32 individuals with large B cell lymphoma treated with either of two CD19 CAR-T products: axicabtagene ciloleucel (axi-cel) or tisagenlecleucel (tisa-cel). Expansion of proliferative memory-like CD8 clones was a hallmark of tisa-cel response, whereas axi-cel responders displayed more heterogeneous populations. Elevations in CAR-T regulatory cells among nonresponders to axi-cel were detected, and these populations were capable of suppressing conventional CAR-T cell expansion and driving late relapses in an in vivo model. Our analyses reveal the temporal dynamics of effective responses to CAR-T therapy, the distinct molecular phenotypes of CAR-T cells with differing designs, and the capacity for even small increases in CAR-T regulatory cells to drive relapse.

CAR-T cell therapy has revolutionized the treatment of hematologic malignancies, resulting in multiple United States Food and Drug Administration approvals since 2017. However, long-term responses only persist in roughly half of patients^{1,2}. Proposed mechanisms for relapse include tumor resistance to apoptosis^{3,4}, target antigen loss⁵, upregulation of inhibitory receptors and intrinsic T cell deficiencies^{6,7}. For patients with chronic lymphocytic leukemia, a dearth of specific apheresis and CAR-T subpopulations seemed to be important for response⁷. However, thus far, investigation of mechanisms of resistance to CAR-T therapy in aggressive large B cell lymphomas (LBCL) has been limited.

The first two Food and Drug Administration-approved CAR-T cell products for LBCL—axicabtagene ciloleucel (axi-cel) and tisagenlecleucel (tisa-cel)—utilize similar CAR designs with identical extracellular binding domains. They have, however, differing manufacturing processes and costimulatory domains (CD28 and 4-1BB respectively), endowing them with different expansion and phenotypic characteristics while maintaining comparable clinical efficacy⁸. CD19 loss has been reported in roughly 30% of lymphoma relapses⁹, suggesting that other factors may explain most cases of nonresponse or relapse. A recent study of single-cell

RNA-sequencing (scRNA-seq) data on cellular infusion products (IP) from LBCL patients treated with axi-cel identified an association between complete clinical response and higher frequencies of CD8 T cells expressing memory signatures, whereas poor clinical response was associated with CD8 T cell exhaustion¹⁰. Much, however, remains to be understood with respect to how transcriptional mechanisms of response vary by product, evolve after infusion into the patient, or fit into the broader context of the host immune system.

We hypothesized that studying the evolutionary trajectories of patient-derived T cells and CAR-T cells from two different CAR products would yield insights into their respective modes of success or failure. Here, we performed scRNA-seq and single-cell T cell receptor (TCR) sequencing of 105 samples from 32 patients with LBCL treated with axi-cel or tisa-cel, collected over the course of treatment. We found substantial differences in the cellular dynamics of response between the two products: tisa-cel responses were associated with striking expansion of rare CD8⁺ central-memory-like populations from the IPs, whereas axi-cel treatment revealed less shifting of T cell lineages between IPs and post-treatment. In axi-cel IPs, we identified increased frequencies of CAR-T regulatory

¹Harvard Graduate Program in Biophysics, Harvard University, Cambridge, MA, USA. ²Cancer Program, The Broad Institute, Cambridge, MA, USA. ³Cancer Center, Massachusetts General Hospital, Boston, MA, USA. ⁴Harvard Medical School, Boston, MA, USA. ⁵Department of Medical Oncology, Dana-Farber Cancer Institute, Boston, MA, USA. ⁶Department of Haematology, University College London Hospitals, London, UK. ⁷Program in Computational Biology and Quantitative Genetics, Harvard T.H. Chan School of Public Health, Boston, MA, USA. ⁸IBM Research, New York, NY, USA. ⁹These authors contributed equally: Nicholas J. Haradhvala, Mark B. Leick, Katie Maurer, Satyen H. Gohil. ¹⁰These authors jointly supervised this work: Catherine J. Wu, Gad Getz, Marcela V. Maus. ✉e-mail: cwu@partners.org; gadgetz@broadinstitute.org; mvmaus@mgh.harvard.edu

(CAR-T_{reg}) cell populations in patients lacking clinical responses. We then showed, through in vitro and in vivo modeling, that these CAR-T_{reg} cells, expressing either product, can suppress conventional CAR-T activity and thus facilitate relapse.

Results

We performed scRNA-seq on peripheral blood mononuclear cells (PBMC) collected from multiple timepoints from 32 individuals with LBCL treated with axi-cel ($n=19$) and tisa-cel ($n=13$), along with their matching IP (Fig. 1a,b and Supplementary Tables 1 and 2). Patient outcomes were tracked for up to 6 months, with fluorodeoxyglucose positron emission tomography (PET) scans taken for clinical response at around 1, 3 and 6 months postinfusion for most patients. We observed 15 of 32 (47%) patients progress or relapse within the 6-month window of observation, consistent with the known clinical activity of these agents (Fig. 1b). We analyzed PBMCs collected within 30 days before treatment ($n=20$ total, $n=12$ at day -30 , $n=4$ at day -5 and $n=4$ on the day of infusion) and, to capture peak CAR-T expansion, also at 7 days (D7) after treatment ($n=29$). When possible, D7 cells were sorted by flow cytometry based on expression of CAR to generate an enriched fraction of CAR-T cells ($n=22$) (Extended Data Fig. 1a; and Methods). Altogether, our cohort yielded a total of 602,577 high-quality cells.

Cells with an in silico detected CAR transcript (Methods) were present at high numbers in the IPs and the sorted CAR⁺ D7 samples, whereas they were only minimally detected in the sorted CAR-fractions and unsorted samples from D7 post-treatment samples (Fig. 1c). In pretreatment samples, we only artifactually detected the CAR transcript in 73 of 131,000 cells (0.0006%).

Clustering of all cells in our dataset enabled the identification of diverse immune cell types present based on canonical markers (Fig. 1d and Extended Data Fig. 1b). Such analysis revealed D7 non-CAR-T cells to intersperse with those from baseline, whereas D7 CAR⁺ cells tended to cluster separately from the baseline and the D7 CAR⁻ cells and IPs clustered independently (Fig. 1d). Most clusters, and in particular the non-T cell clusters, spanned the patients, indicating that there was less variability among patients than among types of cells (Fig. 1d). We observed distinct clustering of the CAR⁺ cells originating from the IP cells, as well as the D7 CAR-sorted samples (Fig. 1e). As expected, the IP samples and D7 CAR⁺ samples consisted primarily of T cells, whereas baseline and D7 CAR⁻ samples contained other populations such as macrophages, myeloid, dendritic cells and B cells (Fig. 1d). We did not detect extensive transcriptional differences among cells from patients treated with tisa-cel versus axi-cel at baseline (Fig. 1d). However, cells from the IPs and D7 samples seemed to cluster by CAR construct and expression, suggesting potential CAR-driven differences in their phenotype (Fig. 1e).

Transcriptomic evolution of CAR-T cells from IP to D7. To explore molecularly the observed separation between transduced CAR-T cells and untransduced T cells, we devised a pseudobulk differential expression approach, which has been shown to help avoid inflated test statistics associated with repeatedly measuring many cells from a comparatively small number of patients¹¹. We performed in silico sorting of cells of each sample into populations of interest (CD4/CD8, CAR/non-CAR) and then aggregated transcripts across all cells of a particular cell type to yield a sample by gene matrix of transcript counts as one might obtain from bulk sequencing (Fig. 2a; and Extended Data Fig. 1c; and Methods).

At D7, we found 463 genes to be elevated (false discovery rate (FDR)<10%, >twofold increase in CAR⁺ cells relative to CAR⁻) in both types of CAR-transduced T cells (Supplementary Table 3), including genes related to cellular proliferation (*DIAPH3*, *BUB1B*, *KIF23*, FDR-corrected *P* value (*Q*)<10⁻⁵ for both products) and activation (for example, *CD109* with log₂ fold change (LFC)=1.3,

Q=2.1×10⁻⁷ and LFC=2.4, *Q*=1.0×10⁻⁷ for tisa- and axi-cel, respectively). Additional genes were found in product-specific analyses, such as increased expression of *CTLA4* in axi-cel IPs (LFC=2.3, *Q*=5.0×10⁻⁵; Fig. 2b).

Our analysis of tisa-cel IPs yielded just one significant hit (*Q*<0.1), likely due to power limitations from the lower CAR transcript detection rate compared with axi-cel (Fig. 1c and Fig. 2b): *ENPP2* (LFC=1.09, *Q*=0.02), which is associated with a 4-1BB signature¹². Indeed, we found genes of this signature to be recurrently upregulated in tisa-cel IPs over axi-cel (Fig. 2c). We observed a subset of these genes maintained expression at D7 (genes in the MHC II pathway), whereas others (such as the transcription factor-encoding *BATF3*) were transiently expressed in the IP but downregulated posttransfusion.

To further map out these temporal transcriptional changes, we calculated differentially expressed genes between IP and D7 for each product separately (Fig. 2d and Supplementary Table 4). Some of the upregulated genes found exclusively in one product reflected known differences between CD28 and 4-1BB signaling in tisa-cel and axi-cel. Consistent with rapid activation associated with CD28 signaling, CD8⁺ axi-cel cells showed stronger upregulation of activation marker *PDCD1* (refs. 13–15) (PD-1, LFC=2.74 D7 relative to IP, *Q*=6.2×10⁻⁷) and checkpoint regulator *SLAMF6* (Fig. 2e; LFC=1.74, *Q*=6.4×10⁻⁷), perhaps suggestive of an early exhaustion signature in this rapidly expanding product¹⁶. We also observed upregulation of *SOS1* in the IP of axi-cel, which is associated with CAR proliferation¹⁷ (*LFC*=−1.97, *Q*=4.8×10⁻⁷).

We identified 1,442 differentially expressed genes shared between the products (708 upregulated and 734 downregulated by at least twofold in D7 samples compared with IP with *Q*<0.1). This included *ZBP1* (tisa-cel LFC=5.7 and *Q*=5.1×10⁻⁹, and axi-cel LFC=3.7 and *Q*=1.7×10⁻¹⁰), which plays an important role in mediating necroptosis in response to interferon-exposed cells¹⁸, suggestive of potential upregulation of activation-induced cell death pathways in both products at this timepoint. *ZBP1*-deficient mice resist systemic inflammation driven by elevations in interferon (IFN) γ signaling, suggesting a potential pathway for regulation of CAR toxicity^{18,19}. Genes lowered in expression at D7 included (1) *IRF4* (tisa-cel LFC=−1.8, *Q*=2.0×10⁻⁹, and axi-cel LFC=−1.8, *Q*=3.4×10⁻⁸) implicated in prevention of exhaustion in the CAR-T cells of in vivo cancer models²⁰; and (2) *CISH* (tisa-cel LFC=−5.6, *Q*=9.8×10⁻¹³, and axi-cel LFC=−5.3, *Q*=4.5×10⁻¹¹), which has been identified as encoding a critical T cell immune checkpoint, the ablation of which results in enhanced T cell function mediated through the TCR²¹.

Associations of cell subsets with clinical response. We next queried our dataset for cell types with frequencies associated with clinical response, defined by whether progressive disease was observed by PET within 6 months of follow up (Methods). Among the CAR⁺ PBMCs, we used the method scCODA²² to test whether any non-T cell populations changed in frequency relative to the number of T cells. We included as covariates treatment product and, for baseline analyses, the timepoint of sampling (days 0, −5 or −30), as we observed that T cell fractions were higher in day 0 samples (Extended Data Fig. 1d). Other factors such as baseline tumor volume were not observed to associate (Extended Data Fig. 1e). We identified monocytes as more abundant in nonresponders at baseline for both products (FDR=0.02, estimated LFC of 0.77 with a 95% high density interval of (0.24,1.31) between nonresponders and responders; Extended Data Fig. 2a), in agreement with previously described results²³. This effect was not observed at D7, nor were any other non-T cell populations found to be significantly altered.

Assessing whether the relative fractions of CD4⁺ and CD8⁺ subsets were associated with response, we found that in patients treated with tisa-cel, but not axi-cel, response was associated with

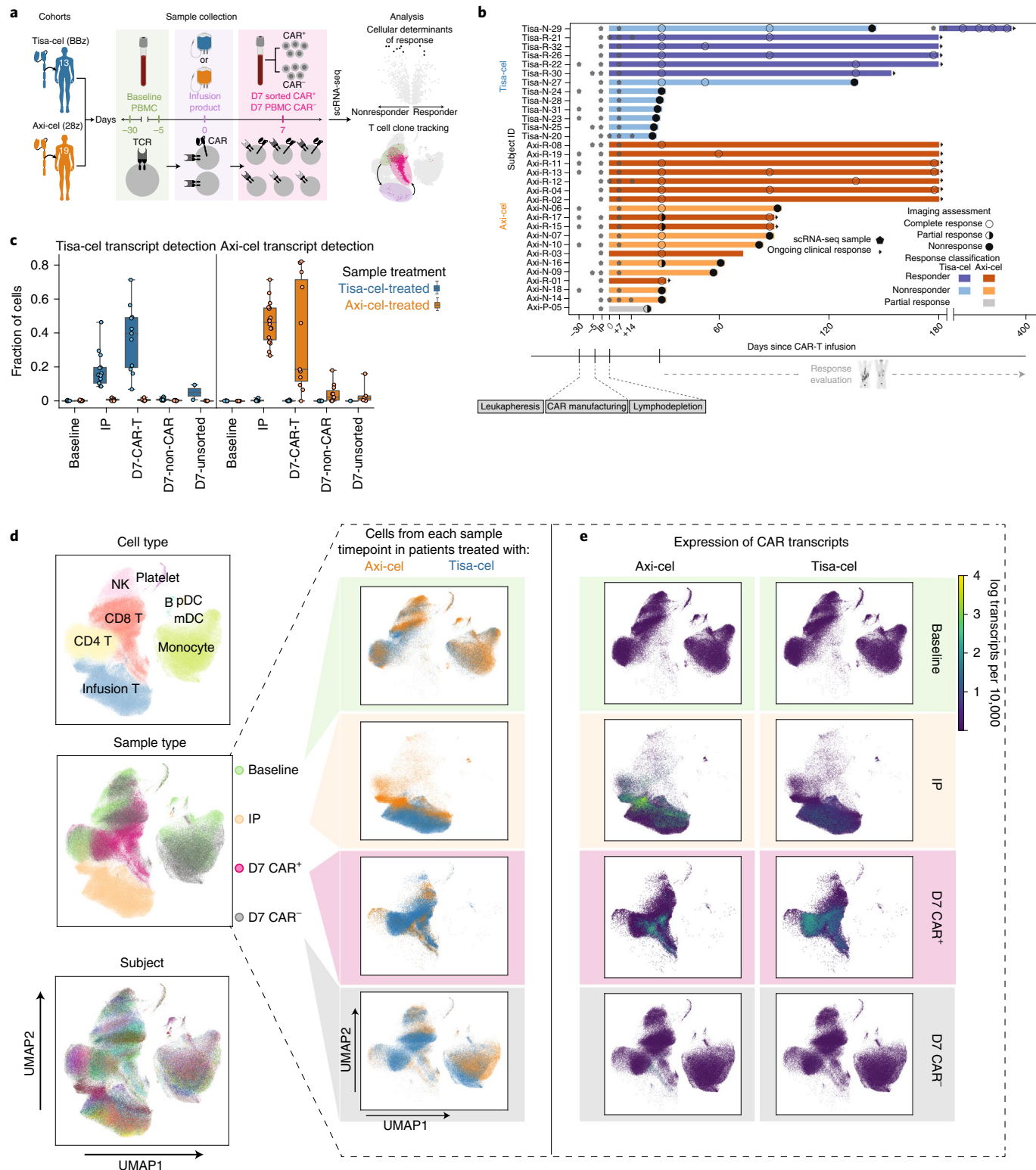


Fig. 1 | The landscape of CAR-T and host immune populations in CAR-T treated patients. **a**, Illustration of study design of treatment with tisa-cel (BBz) or axi-cel (28z). D7, day 7 post-treatment. **b**, Swimmer plot of patient outcomes. Bars represent follow up window (PET scan or physician report), circles represent outcome of PET scans and arrows represent ongoing response. Stars designate timepoints at which samples were collected for scRNA-seq; $n=32$ patients are shown. **c**, Fraction of cells per sample with at least one detected tisa-cel or axi-cel transcript. Each circle represents a sample, and samples from patients treated with tisa-cel or axi-cel are stratified; $n=20$ baseline, $n=11$ IP, $n=22$ D7 CAR⁺, $n=22$ D7 CAR⁻ and $n=7$ D7 unsorted biologically independent samples are shown. The timepoint and sorting strategy is denoted on the x axis. Boxes show the median, interquartile range, and maximum and minimum values. **d,e** UMAP representation of full dataset. On the left, colored by cell type, timepoint and subject. On the right, cells from the same UMAP subset for each timepoint are colored by CAR treatment (orange, axi-cel; blue, tisa-cel) (**d**) and colored by the expression (log transcripts-per-10,000) of each CAR construct detected in each cell (**e**).

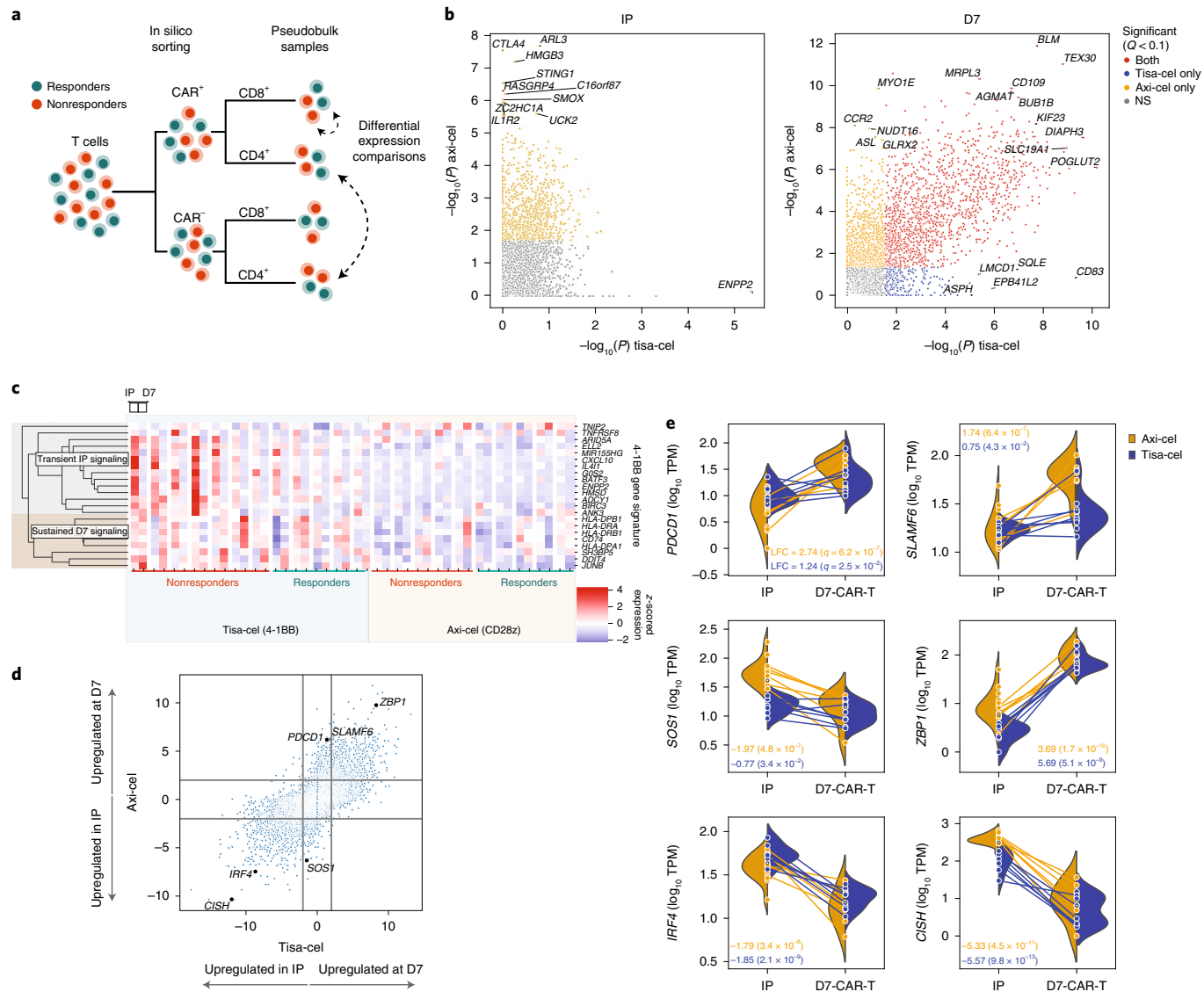


Fig. 2 | Pseudobulk analysis of genes related to treatment, timepoint and response. **a**, Schematic of pseudobulk approach. T cells from IP and D7 samples are in silico sorted for CAR⁺ and CAR⁻ cells and, when stated, CD4 and CD8. Transcript counts are then combined across these cells into one pseudobulk observation. Different conditions are then compared using limma⁴⁸. **b**, Scatterplot of two-tailed $-\log_{10} P$ values derived from moderated *t*-statistics calculated by the limma package testing differential expression between CAR⁺ and CAR⁻ (not separating CD4 and CD8) pseudobulk samples from the IP (left, $n=13$ and $n=18$ for tisa-cel and axi-cel, respectively) and D7 PBMCs (right, $n=13$ and $n=15$) for each product. Genes with Benjamini-Hochberg corrected P values (Q values) of < 0.1 are colored (plotted values are uncorrected). NS, nonsignificant. **c**, Expression of previously identified signature of 4-1BB CAR activation across timepoints and patients. Values are z-scored across patients. **d**, Comparison of genes differentially expressed between CD8⁺ cells in the infusion products ($n=7$ and $n=15$ for tisa-cel and axi-cel, respectively) and at D7 ($n=10$ and $n=7$ for tisa-cel and axi-cel). The scatterplot shows the signed $\log_{10} P$ values obtained from limma testing differences between IP and D7 samples for tisa-cel (x axis) and axi-cel (y axis). Positive values indicate higher expression at D7, and negative values higher in the IP. Gray lines show a significance threshold of $Q=0.01$ for both up- and down-regulated genes on each axis. **e**, Illustration of several highlighted genes in **d**. Lines represent the changes in expression of the gene between IP and day 7 in CD8⁺CAR-T cells of a single sample. Samples are colored by treatment, and split violins represent the distribution of expression across patients of each treatment at a given timepoint. Only samples with 25 or more cells are shown, including $n=22$ IP and $n=17$ D7 CAR⁺ biologically independent samples. Boxes show the interquartile range.

the extent to which D7 CAR⁺ cells were predominantly (>50%) of CD8⁺ subtype (Fig. 3a and Extended Data Fig. 2b,c; likelihood ratio test $P=0.02$ and $P=0.51$ for tisa-cel and axi-cel, respectively). Five out of seven tisa-cel treated patients with lower proportion (<50%) of CD8⁺CAR⁺ T cells at D7 exhibited progressive disease by day 30, and the remaining two relapsed 6 months following treatment. In contrast, only one out of six patients (Tisa-N-31) with greater than 50% CD8⁺CAR-T cells at D7 exhibited progressive disease. The

percentage of CD8⁺ cells in tisa-cel IPs was low in both responders and nonresponders, but had a modest association with 6-month response (Extended Data Fig. 2b; $Q=0.11$).

The temporal dynamics of these CD8 fractions from IP to D7 were strikingly different between the two treatments. In axi-cel, the fraction of D7 CAR⁺ T cells that were CD8⁺ was variable across patients, and this value was highly correlated with the percentage of CD8⁺ cells in the IP (Fig. 3b; Spearman $\rho=0.73$, $P=0.002$). Tisa-cel

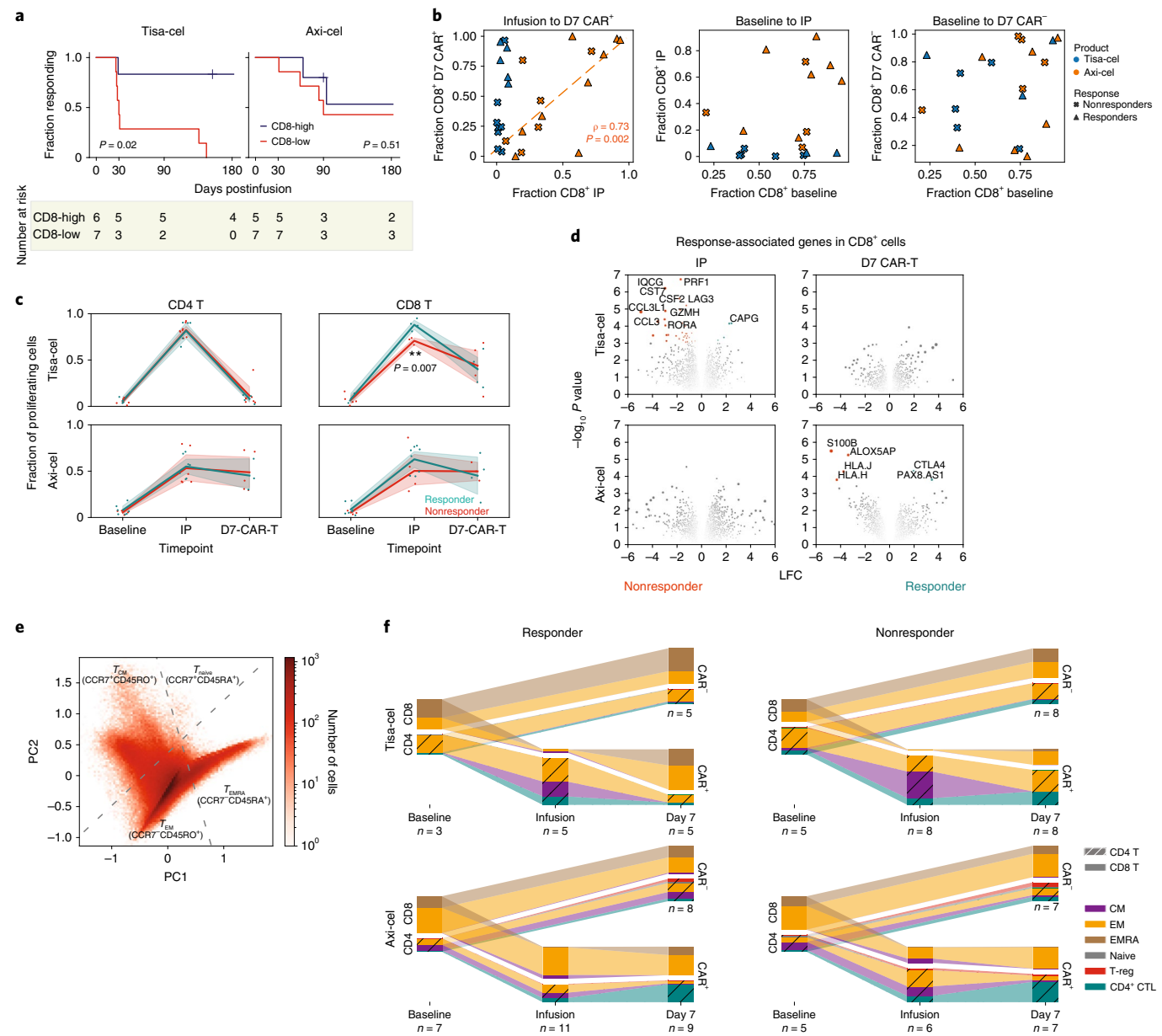


Fig. 3 | Temporal evolution of T cells in responders and nonresponders of different products. **a**, Kaplan-Meier response curves stratified by whether patients had greater than 50% CD8 CAR-T cells (out of all CAR-T cells) at D7. *P* values testing the significance of this stratification using a Cox proportional-hazards model are shown. **b**, Changes in CD8 frequency between different timepoints for CAR⁻ and CAR⁺ cells. **c**, Fraction of cycling cells at different timepoints for different CD4/CD8 designations, treatments and response outcomes. A two-tailed *t*-test is shown for tisa-cel CD8⁺ IPs comparing responders and nonresponders (*P* = 0.007, *t*-statistic = −4.3, *n* = 4 and *n* = 3 for responders and nonresponders, respectively). Individual samples are shown as dots, and a line is drawn showing the mean of each timepoint, with an error band showing a 95% confidence interval derived from bootstrapping 1,000 iterations. **d**, Volcano plots of differentially expressed genes in CD8⁺CAR-T cells between responders and nonresponders for each product and timepoint. *P* values were calculated with the limma package two-tailed test of moderated *t*-statistics. All genes with Benjamini-Hochberg FDR-corrected *P* values *Q* < 0.25 are colored and labeled (plotted values are uncorrected). The area of each dot is the absolute value of the LFC times the negative $\log_{10} P$ value. **e**, PCA dimensionality reduction using knn-smoothed expression of T differentiation markers (CD45RO, CD45RA and CCR7) visualizing the classification of T cell subtypes. Dotted lines represent where the cutoffs used to define CCR7⁺ and CD45RA⁺ (smoothed expression values >0.5) fall in the projection. **f**, Depiction of T subset frequencies at each timepoint for each product and response. Bar widths at each timepoint are proportional to the fraction of cells (out of all cells) being classified as a particular subset. CD4 and CD8 cells are stratified, and distinguished with cross-hatching for CD4 subsets.

IPs, however, were universally composed of less than 10% CD8⁺ cells, but these CD8⁺ cells dramatically expanded at D7, particularly in patients exhibiting long-term response (Fig. 3b). The reduced expansion in nonresponders was seen for patients with CD19 positive and negative relapse alike (Extended Data Fig. 2d). Baseline fractions of CD8⁺ cells were found to be predictive of neither those

observed in the circulating CAR⁻ T cell populations nor in the IPs (Fig. 3b).

Response-associated expansion of CD8⁺ cells in tisa-cel. To explore whether these changing CD4/CD8 frequencies could be explained by different proliferative dynamics, we scored our cells

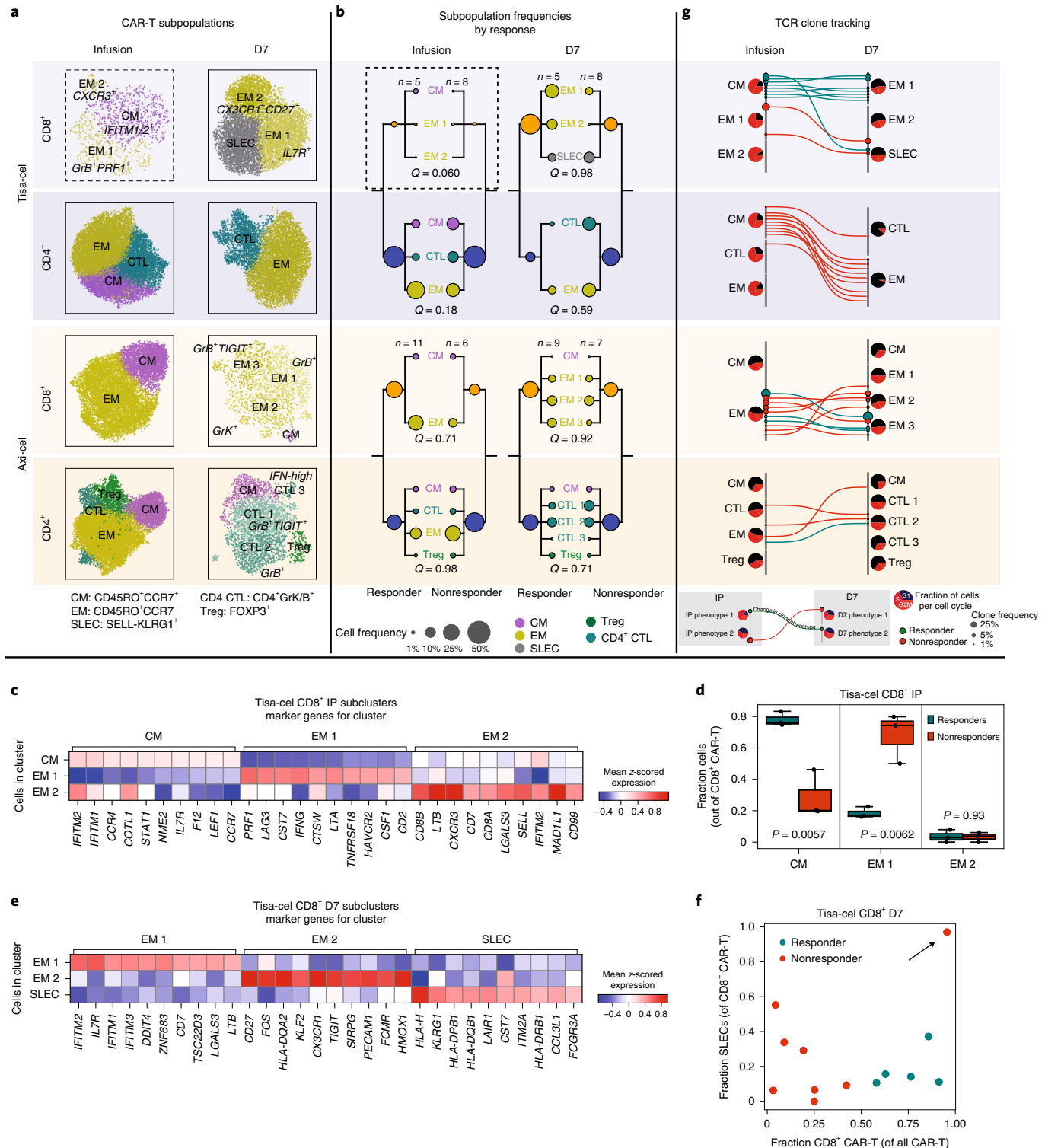


Fig. 4 | Tracking temporal evolution of CAR-T clones by TCR sequencing. **a**, UMAP plots of CAR-T cells of different treatments and at different timepoints colored by subcluster. **b**, Frequencies of CAR-T subclusters. Circle area represents the estimated median percentage of cells belonging to the cluster (out of all CAR-T cells) in patients treated with each product and with each response outcome. Comparison with significant compositional shift between responders and non-responders (log likelihood ratio test $Q < 0.1$; Methods) is highlighted with a box. **c**, Top ten differentially expressed genes in each tis-a cel CD8⁺ IP subcluster, as identified by a t-test. **d**, Relative frequencies of each tis-a cel CD8⁺ IP cluster stratified by response. Only samples with at least 25 CD8⁺CAR-T cells are shown. **e**, Top differentially expressed genes in each tis-a cel CD8⁺ D7 subcluster, as identified by a two-tailed t-test. Biologically independent samples from $n=3$ responders and $n=3$ nonresponders are shown. Boxes show the median, interquartile range, and maximum and minimum values. **f**, Scatterplot of the fraction of CD8⁺ tis-a cel D7 cells in each patient that fell into the SLEC cluster (y axis) versus the overall fraction of CAR-T cells that were CD8⁺ (x axis). Arrow highlights the sole nonresponder to have predominantly CD8⁺ cells are D7. **g**, Up to 15 of the most prevalent TCR clones identified at both timepoints are shown for each CAR-T subset. For each, circles show the cluster in Fig. 3d to which the clone belongs at each timepoint, with sizes corresponding to the clone frequency in its sample. Pie charts show the distribution of cells in each phase of the cell cycle.

for cell cycle gene sets²⁴, and calculated the fraction of cycling CAR-T cells at each timepoint. A higher fraction of cells at a single timepoint in the S and G2/M phases is suggestive that, as a whole, cells in the population are moving faster through G0/G1 (ref. ²⁵), which is the main determinant of proliferation rate. Tisa-cel CD4⁺CAR-T cells exhibited fractions of cycling cells comparable with those of CD8⁺ cells in the IP but essentially no CD4⁺ cells were dividing at D7 (Fig. 3c), explaining the outgrowth of CD8⁺ cells. Responders had higher fractions proliferating CD8⁺ cells in their IPs (two-tailed *t*-test $P=0.007$), likely underlying the greater expansion seen at D7. Meanwhile, axi-cel CD4⁺CAR-T cells exhibited similar proliferation rates to CD8⁺ cells both in the IP and at D7, consistent with them maintaining similar ratios across timepoints.

By testing for genes associated with response in our pseudobulk framework, we found that most differentially expressed genes (14 out of 17 genes with FDR < 10%) were in the CD8⁺ cells of tisa-cel IPs (Fig. 3d and Supplementary Table 5). Nonresponders showed an activated cytotoxic phenotype, with upregulation of genes such as *PRF1* (perforin), *GZMH* and *LAG3*. Thus, further differentiation of these cells provides a possible explanation for the lower proliferation and failure of expansion in nonresponders. We did not observe differential expression when studying CD8⁺ axi-cel IPs. Prior work¹⁰ studying axi-cel IPs had proposed dysfunctional and memory genes characteristic of nonresponders and responders, respectively, but examining these genes in our data did not yield a significant separation of patients by response (Extended Data Fig. 3).

To better characterize the differentiation states of these cells, we developed an expectation–maximization-based method to estimate *CD45RA* and *CD45RO* isoform expression from 5' scRNA data (Extended Data Fig. 4a,b; and Methods). We found in published PBMC datasets with additional feature barcoding of CD45 isoforms that our RNA-based measurements of these isoforms were highly concordant to the surface protein measurements (Extended Data Fig. 4c), and could be used to define T cell subsets similar to those from the protein-derived data (Extended Data Fig. 4d-f). We used smoothed expression of these and other common T cell subset markers (Supplementary Table 6; and Methods) to classify the cells into naive (*CCR7*⁺*CD45RA*⁺), central memory (CM, *CCR7*⁺*CD45RO*⁺), effector memory (EM, *CCR7*⁺*CD45RO*⁺), terminally differentiated effector memory re-expressing *CD45RA* (EMRA, *CCR7*⁺*CD45RA*⁺) and regulatory T cells (*FOXP3*⁺) (Fig. 3e and Extended Data Figs. 4g and 5a-d). We further distinguished CD4⁺ cytotoxic cells (CD4⁺CTLs, *NKG7*⁺), prevalent in our dataset, from other EMs with a more typical helper phenotype (Extended Data Fig. 5b,d).

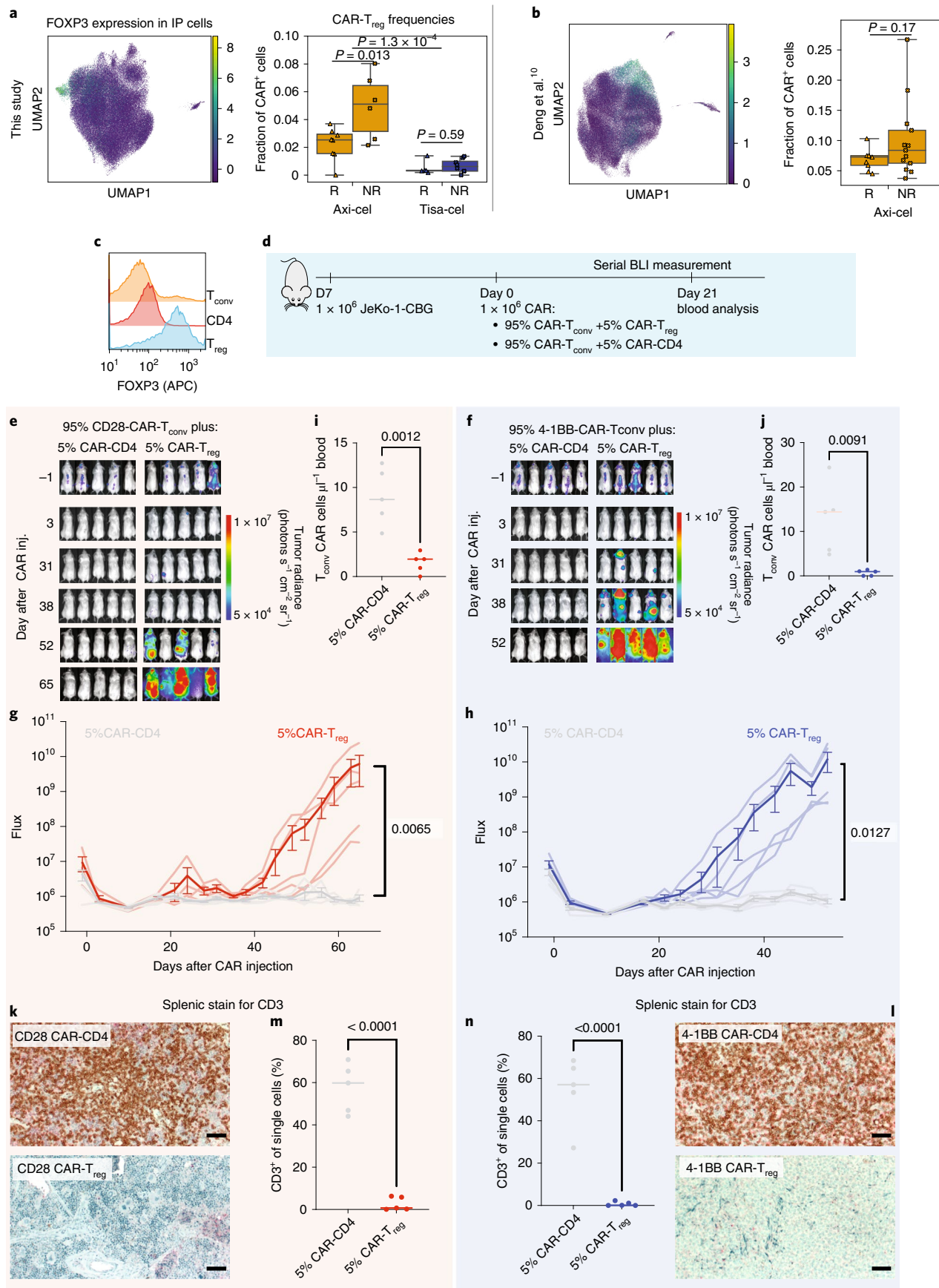
Tisa-cel IPs were composed primarily of CD4⁺ cells with a mix of CM and EM phenotypes, with a modest elevation of CMs in nonresponders compared with responders (Fig. 3f; median of 24% and 56% cells for responders and nonresponders, respectively; two-sided *t*-test $P=0.084$). We observed very few cells classified as Naive in either product (Fig. 3f and Extended Data Fig. 4g), in contrast to the

median of 13.9% seen in the pivotal axi-cel trial²⁶, though consistent with other studies of these products^{27,28}. Due to the stimulation of IP cells during the course of manufacturing, *CD45RA* expression may be modulated to an extent that would affect the classification of cells as CM or Naive, particularly when comparing protein-based with our RNA-based methods.

At D7, CMs were largely replaced by EMs for both products, including CD4⁺CTLs in three of eight of the nonresponding tisa-cel-treated patients (and seen in zero of five responders). The previously noted post-treatment expansion of CD8⁺ cells in tisa-cel took on a primarily *CCR7*⁺*CD45RO*⁺ EM phenotype regardless of response. We observed cells beginning to re-express *CD45RA* (EMRA) in several patients (Extended Data Fig. 5e), although other markers of terminal differentiation were not seen to be elevated (Extended Data Fig. 5f), suggesting they may retain functions similar to EMs. In axi-cel-treated patients, an expansion of CD4⁺CTLs was also seen following treatment (median of 9.2% and 30% of cells in IP and D7 CAR-T populations respectively, *t*-test $P=0.0032$) in responders and nonresponders alike. CAR⁺ cells in patients treated with either treatment were a mix of EM and EMRA phenotypes, which remained unchanged in frequency from baseline to post-treatment (Fig. 3f). T cell subset frequencies at baseline were heterogeneous across patients and mostly not associated with tumor burden or timepoint, with the exception of a depletion of TEMRA cells at day 0 (Extended Data Fig. 1f,g; FDR-corrected rank sum $Q=0.02$).

To further dissect these populations in an unsupervised manner, we performed clustering of IP and D7 CAR-T cells for each treatment and clinical outcome (Fig. 4a and Extended Data Fig. 6a). CD8⁺ tisa-cel IP cells demonstrated a considerable shift in their distribution across the identified clusters when comparing responders and nonresponders (Fig. 4b; log likelihood ratio 20.3, Benjamini-Hochberg-corrected $Q=0.060$; and Methods). Tisa-cel responders had more cells from the cluster expressing CM markers *CCR7* and *LEF1* (two-tailed *t*-test $P=0.0057$; Fig. 4c,d), and expressed the transcription factor *STAT1*. Nonresponders had higher frequencies of cells in cluster EM 1 (two-tailed *t*-test $P=0.0062$) with markers similar to those observed in our pseudobulk analysis: interferon gamma (*IFNG*), perforin (*PRF1*) and markers of activation/exhaustion *LAG3* and *HAVCR2* (TIM-3) (Fig. 4c,d). While overall a shift in the subtypes of CD8⁺ tisa-cel CAR-Ts at D7 was not observed (log likelihood ratio 0.34, $Q=0.98$), we found that the only nonresponder that more than 50% CD8⁺ cells of their CAR-T cells post-treatment (Tisa-N-31) had a phenotype distinct from that of responders in our dataset (Fig. 4e,f). Their cells were distinguished by high expression of *KLRG1* and lack of L-selectin (*SELL*)—a phenotype attributed to short-lived effector cells (SLECs)²⁹. Thus these CD8⁺ cells may not have had the correct phenotype to induce an effective response. This patient had a CD19 positive relapse (Supplementary Table 1), ruling out antigen loss as a potential explanation. The cells of most responders fell into an *IL7R*⁺EM 1 cluster, with the exception of

Fig. 5 | Mediation of relapse by CAR-T_{reg} cells in patients and in vivo validation experiments. a,b Summary of CAR-T_{reg} representation in infusion product cells of this dataset ($n=28$ biologically independent samples with ≥ 100 cells) (a) as well as an independent set of axi-cel infusion products ($n=22$ biologically independent samples) (b). Shown are a UMAP representation of cells colored by FOXP3 expression (left) and the fraction of identified CAR-T_{reg} cells (out of all CAR-T cells) stratified by product and response (right). Boxes show the median, interquartile range, and maximum and minimum values. R, responders; NR, nonresponders. **c**, Intracellular flow cytometry staining of FOXP3 staining of donor T_{reg} cells, CD4-control T cells and T_{conv} T cells. **d**, Schematic of in vivo CAR-T_{reg} validation. NSG mice were injected with 1×10^6 Jeko-CBG lymphoma cells on day -7. On day 0, mice were injected with 1×10^6 CAR-T cells representing 95% CAR-T_{conv} cells with either 5% CAR-T_{reg} cells or 5% CD4⁺CAR-T control cells. Experiment performed with CD19-CD28 (left) or CD19-4-1BB (right) constructs. BLI, bioluminescence imaging. **e-h**, Time course tumor radiance (photons s⁻¹ cm⁻² sr⁻¹) (e,f) and flux (photons s⁻¹) (g,h) for CD28 and 4-1BB experiments, respectively. Mean \pm s.e.m. overlaid on individual subject curves for $n=10$ biologically independent animals treated with each construct. *P* value represents the result of two-way ANOVA. **i,j**, Flow cytometric quantification of CAR-T_{conv} day 14 after CAR injection for $n=10$ biologically independent animals. *P* value represents two-tailed unpaired *t*-test. A line denoting the median value is shown. **k,l**, Representative immunohistochemical staining for human CD3 in the spleen. Scale bars, 100 μ m. **m,n**, Flow cytometric quantification of CD3 cells from the spleens of the indicated conditions for $n=10$ biologically independent animals. *P* value represents two-tailed unpaired *t*-test. A line denoting the median value is drawn.



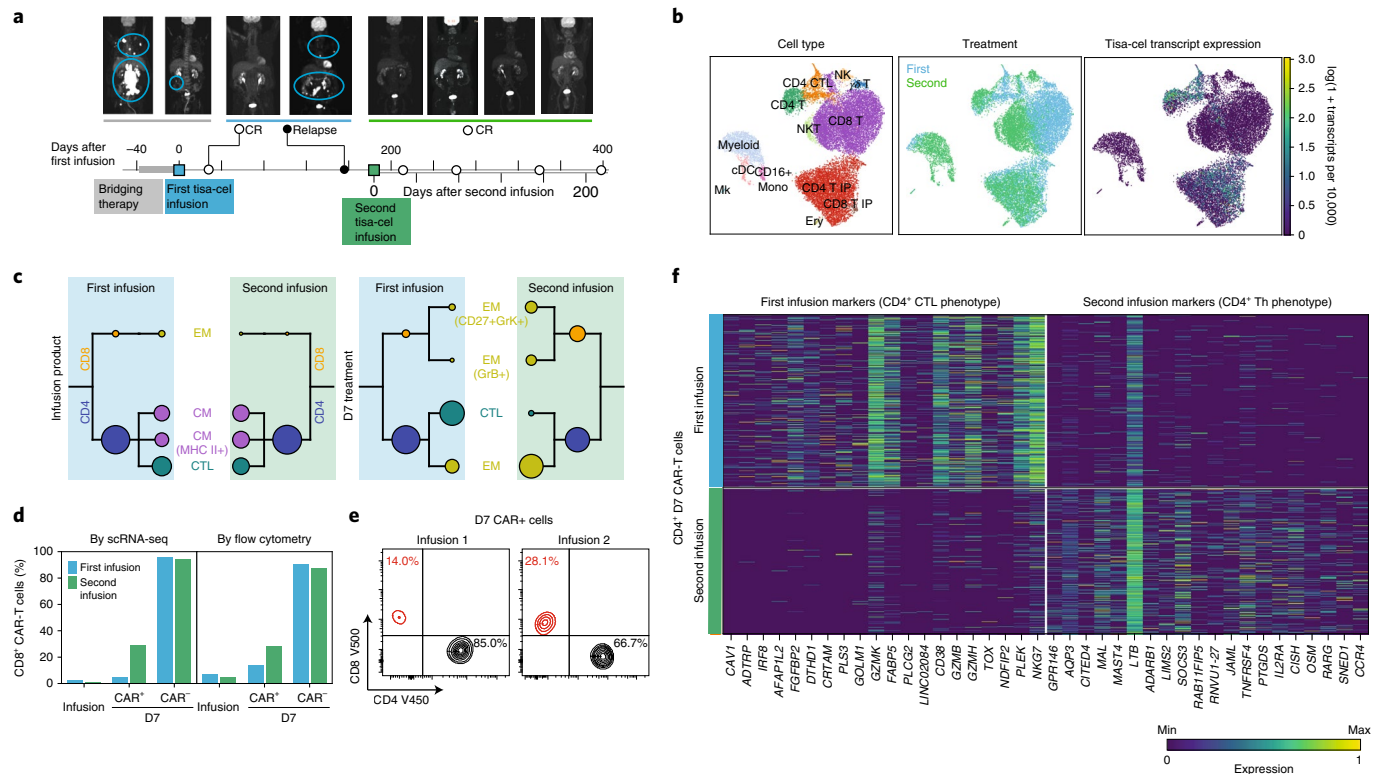


Fig. 6 | Differential characteristics of tisa-cel expansion in patient with relapse and subsequent retreatment. a, PET scans and illustration of treatment timeline for patient with relapse and subsequent retreatment. **b**, UMAP representation of cells from patient with second treatment colored by cell type, first or second infusion, and CAR (tisa-cel) expression. **c**, CAR-T subpopulation frequencies using the same visualization described in Fig. 4b. **d**, Fraction of CD8⁺ cells found by scRNA and flow cytometry in different T cell subsets for each treatment. **e**, Flow cytometric measurements of CD8⁺ cell fractions in day 7 CAR-T cells. **f**, Top differentially expressed genes between the two treatments for CD4⁺CAR-T cells, as determined by a *t*-test. Plotted expression values for each gene are translated and scaled to a range of [0,1].

one patient (Tisa-R-22) with a unique CX3CR1⁺CD27⁺ phenotype (Fig. 4e and Extended Data Fig. 6b; cluster EM 2).

We next used our TCR enrichment libraries to track the temporal evolution of the CAR-T phenotypes. In all tisa-cel responders (and several nonresponders), the top CD8⁺ TCR clones in the IP were found to be increased in frequency at D7 (Extended Data Fig. 6c). In responders, the cluster membership of these clones showed that they originated primarily from CMs in the IP and differentiated into IL7R⁺ EMs at day 7 (Fig. 4g). Meanwhile, clones with a SLEC phenotype at D7 were inferred to have differentiated from the nonresponse-associated GZMB⁺PRF1⁺ EM population. Axi-cel again showed starkly different dynamics, where CM phenotype cells in the IPs exhibited fewer cells in the cell cycle than other IP subsets, and were not observed to be the primary origin of the CAR-T cells present at D7 (Fig. 4g), suggesting a less predominant role, at least initially, of these cells compared with tisa-cel.

Finally, we identified a population of T_{reg} cells with CAR transcripts present (CAR-T_{reg} cells) in the IPs, a rare subset of CD4⁺ circulating lymphocytes that play a critical role in preventing autoimmunity³⁰ but facilitate an immunosuppressive tumor microenvironment in a variety of tumor types, including aggressive lymphomas^{31–35}. However, CAR-T_{reg} cells have not yet been shown to play a role in clinical relapse after CAR-T cell treatment. Analyzing tisa-cel and axi-cel IPs together with batch correction for interproduct differences, we found CAR-T_{reg} cells were significantly rarer in tisa-cel IPs than in axi-cel (Fig. 5a; median 0.3% of all CAR⁺ cells in tisa-cel versus 2.7% in axi-cel, two-tailed *t*-test $P=1.3\times 10^{-4}$). Frequencies of T_{reg} cells at baseline were comparable between patients treated with the two products (Extended Data Fig. 7a;

median of 3.1% and 2.6% of axi-cel and tisa-cel respectively, *t*-test $P=0.21$), suggesting this is not due to pre-existing differences in the patient populations. We also observed other classic markers of T_{reg} cells among the top differentially expressed genes including IL2RA (CD25) and CTLA4 (Extended Data Fig. 7b), providing additional evidence these are genuine T_{reg} cells.

We found that, in axi-cel CAR-T_{reg} cells in IPs, this population had increased frequency in nonresponders (Fig. 5a; two-tailed *t*-test $P=0.013$, median of 5.1% and 2.5% with ranges of 2.2–8% and 0–3.7% in nonresponders and responders, respectively). T cells without a detected CAR had lower fractions of T_{reg} cells (median 0.6%), and they were present at a higher median level in nonresponders (Extended Data Fig. 7a; median 1.5% versus 0.4%, *t*-test $P=0.082$). However, due to the lack of definitive flow cytometric isolation of such CAR-negative cells from our IP samples and the sparsity of scRNA-sequencing data, this increase in nonresponders could be due to contamination by CAR-transduced cells for which we did not detect a CAR transcript. In exploring an external single-cell dataset¹⁰ of axi-cel IPs, we also found a trend towards higher T_{reg} cells in nonresponders (Fig. 5b; two-tailed *t*-test $P=0.17$). Most striking were several nonresponders with very high CAR-T_{reg} frequencies, up to 26.7% of all CAR⁺ cells (range 4.5–10.3% for responders, and 3.7–26.7% for nonresponders).

CAR-T_{reg} cells drive lymphoma relapse in vivo. To assess whether CAR-T_{reg} cells could drive resistance in aggressive lymphomas at the proportions observed in the IPs, we pursued in vitro and in vivo modeling. We isolated bulk-CD3⁺ conventional T cells (T_{conv}), T_{reg} cells and CD4⁺ T cells from healthy donor peripheral blood, and

transduced these populations with either CD28 or 4-1BB costimulated second-generation CD19-targeted CAR constructs (Fig. 5c and Extended Data Fig. 7c,d). By carboxyfluorescein succinimidyl ester staining of the bulk population, a population of 25% CAR-T_{reg} cells reduced CAR-T_{conv} expansion compared with CAR-CD4 controls for both constructs (Extended Data Fig. 7e,f). To assess the contribution of CAR-T_{reg} cells to relapse in an in vivo model of lymphoma, we subjected NSG mice engrafted with JeKo-1 lymphoma cells to injection of CAR-T cells composed of 100% CAR-T_{conv} or 75% CAR-T_{conv} with either 25% CAR-CD4 or 25% CAR-T_{reg} cells (Extended Data Fig. 8a; Methods). All mice seemed to rapidly clear tumor by day 3 (Extended Data Fig. 8b,c). However, for both constructs, the overall numbers of CAR-T_{conv} cells in the peripheral blood at day 14 were suppressed in the CAR-T_{reg} treated mice (Extended Data Fig. 8d,e), and most of the mice treated with products containing CAR-T_{reg} cells relapsed, whereas none of the control mice had at the time of euthanasia on day 35 (Extended Data Fig. 8f,g). Quantification of CAR-T_{conv} cells in the spleen at the time of euthanasia revealed high levels in the CAR-CD4-control mice and minimal levels of CAR-T_{conv} in the mice treated with injections containing CAR-T_{reg} cells (CD28 median 37.0 versus 2.3, $P=0.007$; 4-1BB median 54.1 versus 0.6, $P=0.0003$, Extended Data Fig. 8h-k).

After demonstrating that 25% CAR-T_{reg} cells were sufficient to drive relapse, we next wanted to ascertain whether a lower, more physiologically relevant proportion of CAR-Tregs (as seen in our cohort) could also drive relapse. We engrafted NSG mice with JeKo-1 lymphoma cells followed by injection of CAR-T cells 7 days later, composed of 95% CAR-T_{conv} with either 5% CAR-CD4, or 5% CAR-T_{reg} cells (Fig. 5d). Again, after apparent early tumor clearance in all mice by day 3, all CAR-T_{reg} mice developed frank relapse after extended follow up, whereas no relapses were seen in control mice (Fig. 5e-h). Assessment of peripheral blood CAR-T_{conv} expansion at day 21 revealed suppression in the CAR-T_{reg} treated mice relative to control mice (CD28 median 8.7 versus 2.0, $P=0.0012$; 4-1BB 14.4 versus 0.9 $P=0.0091$; Fig. 5i,j). At the time of euthanasia, splenic CD3 staining was markedly reduced in all CAR-T_{reg} mice by immunohistochemical staining and flow cytometry (CD28 median 59.8 versus 0.68 $P=<0.0001$, 4-1BB median 57.1 versus 0.12, $P<0.0001$; Fig. 5k-n). Thus, CAR-T_{reg} cells making up merely 5% of total infused CAR-T cells were sufficient to drive late tumor relapses and suppress CAR-T_{conv} expansion.

Differential CAR-T populations in patient with reinfusion. One of the study subjects (Tisa-N-29) who received tisa-cel had a CD19⁺ relapse 6 months after treatment. This patient was subsequently treated with a second infusion of the same IP and then achieved clinical and radiographic complete remission (last follow up 215 days after infusion; Fig. 6a).

PBMCs collected 7 days after retreatment as well as the readministered IP were analyzed by scRNA-seq as before (Fig. 6b). As expected, the two IP products lacked any discernible differences in cellular composition (Fig. 6b,c). In contrast, CAR-T cells at D7 following each of the treatments exhibited marked differences. While few (5%) CD8⁺CAR-T cells were detectable 7 days after the initial infusion, around 30% (a sixfold increase) was observed after the second (Fig. 6d)—a finding confirmed by parallel flow cytometry measurements (Fig. 6d,e). Between the two infusions, no differences in phenotype were found in the postinfusion circulating CD8⁺CAR-T cells, although statistical power for this comparison was limited by the low frequency of CD8⁺ T cells after the first treatment. On the other hand, the phenotype of CD4⁺CAR-T cells shifted strikingly from one treatment to the other (Fig. 6c,f). The CAR-T cells had a CTL phenotype after the first infusion, with top differentially expressed genes including markers of cytotoxicity (GZMK, GZMB, GZMH, NGK7), the transcription factor IRF8 and the gene TOX, implicated previously in T cell exhaustion³⁶. In contrast,

CD4⁺ cells after the second infusion instead expressed genes more consistent with a helper phenotype such as TNFRSF4 (encoding the costimulatory molecule OX40) and Th2-marker CCR4.

Differences were also observed in the non-CAR compartment, with the first post-treatment sample being composed of almost exclusively CD8⁺ T cells, whereas the second additionally contained myeloid and natural killer cells (Fig. 6b and Extended Data Fig. 9a,b). The CD8⁺ non-CAR-T cells exhibited substantial differences in expression between the two timepoints. After the first treatment, these cells expressed CD27 and CXCR3. After the second they expressed higher levels of transcription factor-encoding genes GATA3 and TBX21 (t-bet) and increased levels of GNLY (Extended Data Fig. 9c).

Discussion

CD19 CAR-T therapy has provided a cure to roughly 40% of patients with previously incurable lymphomas^{26,37}, but the failure modes in the remaining patients remain incompletely understood^{38–40}. Our study provides important observations of temporal changes in clonal and expression dynamics of the two main CD19 CAR-T designs in use for LBCL (Extended Data Fig. 10). Tisa-cel responses were associated with expansion of central-memory CD8 populations—a phenomenon not seen in axi-cel. Curiously we did not observe the same associations of CM and exhaustion phenotypes with response to axi-cel as found in a previous study¹⁰. Larger cohorts will be needed to understand whether this is due to the still relatively small sample sizes attainable with scRNA-seq, or the result of genuine differences in the patient populations or clinical practices of our respective hospitals.

A striking feature of our data is the divergent phenotypes and apparent response mechanisms of the two products. The two products have differing designs (4-1BB versus CD28 costimulation, CD8 versus CD28 transmembrane for tisa-cel versus axi-cel), are delivered by different vectors and have differing manufacturing processes⁴¹ (fresh versus frozen apheresis products, activation by antibody-coated beads versus soluble antibody and cytokines), although the precise details remain proprietary. Understanding predictive molecular features of response specific to each product will give insights to further optimize their design and manufacturing, and may help identify which product is most likely to succeed in a given patient.

Apart from the CAR-T cells themselves, our case where readministration of a second infusion of the same tisa-cel IP to a patient resulted in expansion of different immune cell populations after each treatment highlights the importance of CAR-T-extrinsic phenotypes in response. How important is the host immunological milieu for CAR-T cell therapy and to what extent can we optimize it? Do the stochastics of infusing individual unique cells matter more than previously thought? Tumor-intrinsic factors such as overall disease burden may also play a role; however, in this case, tumor burden was higher upon the second infusion (Supplementary Table 1; sum of the product diameters values of 37.2 and 58.9 cm² for the first and second dose, respectively). Retrospective studies of patients who have received multiple infusions suggest that this successful reinduction of remission is rare⁴².

Finally, we found that increases in infusional CAR-T_{reg} cells are associated with nonresponse to axi-cel treatment, and demonstrate that similar trends exist in data from a previous study of axi-cel products¹⁰. In vivo modeling suggests that this may be sufficient to drive late relapses and suppression of CAR-T_{conv} expansion in lymphoma, demonstrating that small numbers of CAR-T_{reg} cells are capable of driving clinical relapse. Depletion of T_{reg} cells using CD25 selection has been performed at clinical scale in the context of an autologous stem cell transplant for multiple myeloma⁴³, suggesting that such a step could be added to traditional CAR-T manufacturing pipelines. Additionally, whereas in vivo modeling demonstrated

that CAR-T_{reg} cells incorporating either costimulatory domain could cause relapse, we observed substantially lower numbers of CAR-T_{reg} cells in tisa-cel products. As axi-cel manufacturing begins from fresh apheresis cells whereas tisa-cel is derived from frozen cells, we speculate that cryopreservation may serve as a crude depletion of T_{reg} cells, which are notoriously intolerant of freezing^{44–46}.

We note several aspects not examined by our current manuscript, including the impact of different times of peak expansion (median of 7 and 9 days for axi-cel and tisa-cel), as well as lengths of persistence, with axi-cel rapidly declining while tisa-cel can be detected for months or years after infusion, particularly in responders^{26,37,47}. Furthermore our study was limited to blood, and future investigation of lymph node biopsies and analysis of tumor-CAR-T interactions remains a fruitful avenue for research.

In summary, we have profiled the transcriptomic evolution of immune cells over the course of treating refractory LBCLs with the first two CD19 CAR-T products. It is our hope that through illumination of the response-associated characteristics of each treatment we can optimize the design of CAR-T therapies, match patients with the treatments most likely to induce a clinical response and understand strategies for combating relapse.

Online content

Any methods, additional references, Nature Research reporting summaries, source data, extended data, supplementary information, acknowledgements, peer review information; details of author contributions and competing interests; and statements of data and code availability are available at <https://doi.org/10.1038/s41591-022-01959-0>.

Received: 24 March 2022; Accepted: 19 July 2022;

Published online: 12 September 2022

References

- Maude, S. L. et al. Chimeric antigen receptor T cells for sustained remissions in leukemia. *N. Engl. J. Med.* **371**, 1507–1517 (2014).
- Schuster, S. J. et al. Chimeric antigen receptor T cells in refractory B-cell lymphomas. *N. Engl. J. Med.* **377**, 2545–2554 (2017).
- Singh, N. et al. Impaired death receptor signaling in leukemia causes antigen-independent resistance by inducing CAR T-cell dysfunction. *Cancer Discov.* **10**, 552–567 (2020).
- Dufva, O. et al. Integrated drug profiling and CRISPR screening identify essential pathways for CAR T-cell cytotoxicity. *Blood* **135**, 597–609 (2020).
- Orlando, E. J. et al. Genetic mechanisms of target antigen loss in CAR19 therapy of acute lymphoblastic leukemia. *Nat. Med.* **24**, 1504–1506 (2018).
- Das, R. K., Vernau, L., Grupp, S. A. & Barrett, D. M. Naïve T-cell deficits at diagnosis and after chemotherapy impair cell therapy potential in pediatric cancers. *Cancer Discov.* **9**, 492–499 (2019).
- Fraietta, J. A. et al. Determinants of response and resistance to CD19 chimeric antigen receptor (CAR) T cell therapy of chronic lymphocytic leukemia. *Nat. Med.* **24**, 563–571 (2018).
- Cappell, K. M. & Kochenderfer, J. N. A comparison of chimeric antigen receptors containing CD28 versus 4-1BB costimulatory domains. *Nat. Rev. Clin. Oncol.* **18**, 715–727 (2021).
- Plaks, V. et al. CD19 target evasion as a mechanism of relapse in large B-cell lymphoma treated with axicabtagene ciloleucel. *Blood* **138**, 1081–1085 (2021).
- Deng, Q. et al. Characteristics of anti-CD19 CAR T cell infusion products associated with efficacy and toxicity in patients with large B cell lymphomas. *Nat. Med.* **26**, 1878–1887 (2020).
- Squair, J. W. et al. Confronting false discoveries in single-cell differential expression. *Nat. Commun.* **12**, 5692 (2021).
- Boroughs, A. C. et al. A distinct transcriptional program in human CAR T cells bearing the 4-1BB signaling domain revealed by scRNA-Seq. *Mol. Ther.* **28**, 2577–2592 (2020).
- Zhao, Z. et al. Structural design of engineered costimulation determines tumor rejection kinetics and persistence of CAR T cells. *Cancer Cell* **28**, 415–428 (2015).
- Salter, A. I. et al. Phosphoproteomic analysis of chimeric antigen receptor signaling reveals kinetic and quantitative differences that affect cell function. *Sci. Signal.* **11**, eaat6753 (2018).
- Lindner, S. E., Johnson, S. M., Brown, C. E. & Wang, L. D. Chimeric antigen receptor signaling: functional consequences and design implications. *Sci. Adv.* **6**, eaaz3223 (2020).
- Yigit, B. et al. SLAMP6 as a regulator of exhausted CD8⁺ T cells in cancer. *Cancer Immunol. Res.* **7**, 1485–1496 (2019).
- Wang, Y. et al. Low-dose decitabine priming endows CAR T cells with enhanced and persistent antitumour potential via epigenetic reprogramming. *Nat. Commun.* **12**, 409 (2021).
- Yang, D. et al. ZBP1 mediates interferon-induced necroptosis. *Cell. Mol. Immunol.* **17**, 356–368 (2019).
- Zhan, Y., Carrington, E. M., Zhang, Y., Heinzel, S. & Lew, A. M. Life and death of activated T cells: how are they different from naïve T cells? *Front. Immunol.* **8**, 1809 (2017).
- Seo, H. et al. BATF and IRF4 cooperate to counter exhaustion in tumor-infiltrating CAR T cells. *Nat. Immunol.* **22**, 983–995 (2021).
- Palmer, D. C. et al. Cish actively silences TCR signaling in CD8⁺ T cells to maintain tumor tolerance. *J. Exp. Med.* **212**, 2095–2113 (2015).
- Büttner, M., Ostner, J., Müller, C. L., Theis, F. J. & Schubert, B. scCODA is a Bayesian model for compositional single-cell data analysis. *Nat. Commun.* **12**, 6876 (2021).
- Jain, M. D. et al. Tumor interferon signaling and suppressive myeloid cells are associated with CAR T-cell failure in large B-cell lymphoma. *Blood* **137**, 2621–2633 (2021).
- Tirosh, I. et al. Dissecting the multicellular ecosystem of metastatic melanoma by single-cell RNA-seq. *Science* **352**, 189–196 (2016).
- Kafri, R. et al. Dynamics extracted from fixed cells reveal feedback linking cell growth to cell cycle. *Nature* **494**, 480–483 (2013).
- Neelapu, S. S. et al. Axicabtagene ciloleucel CAR T-cell therapy in refractory large B-cell lymphoma. *N. Engl. J. Med.* **377**, 2531–2544 (2017).
- Talleur, A. et al. Preferential expansion of CD8⁺ CD19-CAR T cells postinfusion and the role of disease burden on outcome in pediatric B-ALL. *Blood Adv.* <https://doi.org/10.1182/bloodadvances.2021006293> (2022).
- Monfrini, C. et al. Phenotypic composition of commercial anti-CD19 CAR-T cells affects in vivo expansion and disease response in large B-cell lymphoma patients. *Clin. Cancer Res.* <https://doi.org/10.1158/1078-0432.CCR-22-0164> (2022).
- Martin, M. D. & Badovinac, V. P. Defining memory CD8 T cell. *Front. Immunol.* **9**, 2692 (2018).
- Sakaguchi, S., Yamaguchi, T., Nomura, T. & Ono, M. Regulatory T cells and immune tolerance. *Cell* **133**, 775–787 (2008).
- Lee, J. C. et al. In vivo inhibition of human CD19-targeted effector T cells by natural T regulatory cells in a xenotransplant murine model of B cell malignancy. *Cancer Res.* **71**, 2871–2881 (2011).
- Todo, S. et al. A pilot study of operational tolerance with a regulatory T-cell-based cell therapy in living donor liver transplantation. *Hepatology* **64**, 632–643 (2016).
- Chandran, S. et al. Polyclonal regulatory T cell therapy for control of inflammation in kidney transplants. *Am. J. Transpl.* **17**, 2945–2954 (2017).
- Broughs, A. C. et al. Chimeric antigen receptor costimulation domains modulate human regulatory T cell function. *JCI Insight* **5**, e126194 (2019).
- Togashi, Y., Shitara, K. & Nishikawa, H. Regulatory T cells in cancer immunosuppression—implications for anticancer therapy. *Nat. Rev. Clin. Oncol.* **16**, 356–371 (2019).
- Khan, O. et al. TOX transcriptionally and epigenetically programs CD8⁺ T cell exhaustion. *Nature* **571**, 211–218 (2019).
- Schuster, S. J. et al. Tisagenlecleucel in adult relapsed or refractory diffuse large B-cell lymphoma. *N. Engl. J. Med.* **380**, 45–56 (2019).
- Shah, N. N. & Fry, T. J. Mechanisms of resistance to CAR T cell therapy. *Nat. Rev. Clin. Oncol.* **16**, 372–385 (2019).
- Brown, C. E. & Mackall, C. L. CAR T cell therapy: inroads to response and resistance. *Nat. Rev. Immunol.* **19**, 73–74 (2019).
- Larson, R. C. & Maus, M. V. Recent advances and discoveries in the mechanisms and functions of CAR T cells. *Nat. Rev. Cancer* **21**, 145–161 (2021).
- Zhang, J. et al. A review of two regulatory approved anti-CD19 CAR T-cell therapies in diffuse large B-cell lymphoma: why are indirect treatment comparisons not feasible? *Adv. Ther.* **37**, 3040–3058 (2020).
- Gauthier, J. et al. Factors associated with outcomes after a second CD19-targeted CAR T-cell infusion for refractory B-cell malignancies. *Blood* **137**, 323–335 (2021).
- Derman, B. A. et al. Regulatory T-cell depletion in the setting of autologous stem cell transplantation for multiple myeloma: pilot study. *J. Immunother. Cancer* **8**, e000286 (2020).
- Golab, K. et al. Challenges in cryopreservation of regulatory T cells (Tregs) for clinical therapeutic applications. *Int. Immunopharmacol.* **16**, 371–375 (2013).
- Florek, M. et al. Freeze and thaw of CD4⁺CD25⁺Foxp3⁺ regulatory T cells results in loss of CD62L expression and a reduced capacity to protect against graft-versus-host disease. *PLoS ONE* **10**, e0145763 (2015).

46. Gołęb, K. et al. Cell banking for regulatory T cell-based therapy: strategies to overcome the impact of cryopreservation on the Treg viability and phenotype. *Oncotarget* **9**, 9728–9740 (2018).
47. Melenhorst, J. J. et al. Decade-long leukaemia remissions with persistence of CD4⁺ CAR T cells. *Nature* **602**, 503–509 (2022).
48. Ritchie, M. E. et al. limma powers differential expression analyses for RNA-sequencing and microarray studies. *Nucleic Acids Res.* **43**, e47 (2015).

Publisher's note Springer Nature remains neutral with regard to jurisdictional claims in published maps and institutional affiliations.

Springer Nature or its licensor holds exclusive rights to this article under a publishing agreement with the author(s) or other rightsholder(s); author self-archiving of the accepted manuscript version of this article is solely governed by the terms of such publishing agreement and applicable law.

© The Author(s), under exclusive licence to Springer Nature America, Inc. 2022

Methods

Patient samples and cell preparation. All patients were treated with commercial CAR-T cell products; clinical data and blood samples were obtained after written informed consent under an Institutional Review Board-approved protocol at the Dana-Farber/Harvard Cancer Center (DFHCC No. 16-206 and 17-561). We complied with all relevant ethical regulations for human research participants. No compensation was provided for participation. Demographic information (age and gender) are provided in Supplementary Table 1. Responders were defined as those without radiographic relapse by 6 months of follow up. Nonresponders were defined as patients whose disease either did not have an initial response at day 28 or who progressed before the 6-month follow up window. Infusion products were collected from the remnants of infusion bags and cryopreserved in a solution of 10% dimethylsulfoxide in fetal bovine serum (FBS). Tumor burden was assessed using sum of the product diameters, which is based on revised International Working Group response criteria for malignant lymphoma^{19,50} and has previously been utilized for tumor burden assessment in lymphoma patients treated with CAR-T cell therapy^{26,51}.

Cryopreserved PBMC from D7 after CAR-T infusion were thawed and resuspended in flow cytometry staining buffer (FACS) (PBS with 2% FBS); 5 μl of Fc block (BD Bioscience) was added for 5 min followed by addition of the antibodies in BD brilliant stain buffer (BD Bioscience). The cells were stained for 20 min at 4°C using the following antibody clones: CD45 (BV786 BD HI30 563716) used at dilution of 1 in 167, CD3 (APC BD Biosciences catalog no. 5H3 340661) used at dilution of 1 in 83.5, CD4 (V450 BD Bioscience catalog no. SK3 651850) used at dilution of 1 in 83.5, CD8 (V500c BD Bioscience catalog no. SK1 647458) used at dilution of 1 in 83.5, CD14 (FITC BD Bioscience catalog no. Mqp9 347493) used at dilution of 1 in 83.5 and sCD19-PE (BioLegend custom conjugation catalog no. 900002598, lot B324342) used at dilution of 1 in 55.6. Cells were then washed twice and resuspended in FACS buffer followed by addition of 7AAD (BioLegend). Live CAR-T cells and non-CAR-T cells were acquired separately using a BD FACSAria utilizing the gating strategy in Extended Data Fig. 1a with gating based on healthy non-CAR-transduced donor PBMC prepared separately for each batch. Samples were resuspended in 0.04% ultrapure bovine serum albumin in PBS at 1,000 cells μl⁻¹ density before loading on a 10x Genomics Chromium platform. Infusion product and baseline samples were thawed similarly and combined into batches of up to four samples per 10x channel loaded at a density of 3,000 cells μl⁻¹. For some infusion product samples with a poor postthaw viability (<80%), the Miltenyi Dead Cell Removal kit (130-090-101) was used to deplete dead cells before scRNA-seq.

Single-cell transcriptome sequencing data generation. Viable cells were resuspended in PBS with 0.04% BSA at a cell concentration of 1,000 cells μl⁻¹. A total of 40,000 cells were loaded onto a 10x Genomics Chromium instrument (10x Genomics) according to the manufacturer's instructions. The scRNA-seq libraries were processed using Chromium single-cell 5' library and gel bead kit v.2 and coupled scTCR-seq libraries were obtained using Chromium single-cell V(D)J enrichment kit (human T cell) (10x Genomics). Quality control for amplified cDNA libraries and final sequencing libraries was performed using Bioanalyzer High Sensitivity DNA Kit (Agilent). Both scRNA-seq and scTCR-seq libraries were normalized to 4 nM concentration and pooled in a volume ratio of 4:1. The pooled libraries were sequenced on Illumina NovaSeq S4 platform. The sequencing parameters were: Read 1 of 26 bp, Read 2 of 90 bp, index 1 of 10 bp and index 2 of 10 bp.

Generation of CAR reference. A custom reference was built using GRCh38 and the Ensembl 100 annotation, supplemented with sequences for both the axi-cel and tisa-cel constructs. To determine the sequence of these constructs, we created an initial reference including the sequences of pELPs 19-BBz⁵² for tisa-cel, and msgv-fmc63-28z⁵³ for axi-cel. We then aligned read two of four of our infusion product samples (Tisa-R-21, Tisa-N-20, Axi-R-1, Axi-N-14) to this supplemented genome using STAR v.2.5.1b. We used the bcftools call tool (v.1.11) to identify variants of the true CAR sequence from our initial reference, and the bcftools consensus tool to create an updated fasta file with refined CAR sequences. This was then added to our GRCh38-based reference and prepared with Cellranger mkref (v.6.0.1) giving the reference genome used for preprocessing of the full dataset.

Preprocessing of scRNA-seq GEX data. Raw fastq files for all 10x runs were aligned and quantified using Cellranger v.6.0.1 with the 'expect cells' parameter set to 5 × 10³ per pooled sample (for example a run with five multiplexed samples was set to 2.5 × 10⁴) and using the custom reference described above. Gene expression matrices were further filtered for ambient contamination using cellbender v.0.2.0.

For all cell multiplexed samples, we ran souporcell v.2020.7 to identify genotype clusters using the 1000 genomes common (>2% allele frequency) single nucleotide polymorphism sites. The genotype of every patient at these sites was identified by running bcftools call on the CAR-sorted D7 samples (since these were not multiplexed). The identity of genotype clusters was the reidentified by finding the patient with the least discordant genotype calls expected to be in the pool. TCR sequencing data for all runs was processed using cellranger vdj (v.6.0.1) and the GRCh38_vdj_v5.0 reference package.

Classification of cell types. An initial clustering of the cells was performed using scanpy⁵⁴ v.1.8.1 and a standard single-cell workflow. Doubts were filtered by running scrublet⁵⁵ v.0.2.1 on each 10x channel individually for PBMC samples. Cells were filtered for a minimum of 200 genes and less than 15% mitochondrial RNA transcripts. Data was log-normalized for each cell as $\ln(1 + 10^n_g/N)$ where n_g represents the number of UMIs detected in gene g out of N total UMIs detected in the cell. Variable genes were selected using scanpy's highly_variable_genes process with a minimum dispersion of 0.2 and mean expression values between 0.01 and 3. We further blacklisted from clustering consideration the axi-cel and tisa-cel genes, any TCR or BCR variable genes, as well as sex-biased genes XIST, RPS4Y1 and RPS4Y2. We regressed out the effects of total unique molecular identifiers (UMI) counts and mitochondrial RNA percentages, and then standardized the expression values with a maximum of ten. We performed principal component analysis (PCA), then used Harmony v0.05⁵⁶ to integrate our data batches. Nearest neighbors were computed using the top 18 Harmony-adjusted principal components (PCs), and uniform manifold approximation and projection (UMAP) was run to produce the global visualizations shown.

Classification of CD4 and CD8 populations. Due to scRNA sparsity, CD4 and CD8 T cells cannot be classified directly by gene expression, and clustering at reasonable resolutions did not always cleanly separate these populations. To overcome this, we computed a nearest-neighbor graph using $k=100$. We then calculated smoothed expression of CD4 and CD8A by taking the mean across the 100 nearest neighbors of every cell. We then classified CD4 and CD8 T cells by gating on these expression values (Extended Data Fig. 1c).

Quantification of CD45 isoform expression. Because the important splicing events to distinguish CD45RA and CD45RO isoforms occur at the 5' end of the gene (exons 4–7), we were able to develop an isoform quantification model similar to those commonly employed in bulk RNA-sequencing⁵⁷. First for every read, we calculated a binary matrix of values $C_{r,i}$ which are 1 if splicing of read r was compatible with each of the six human isoforms i of CD45 (RO, RA, RAB, RB, RBC, RABC). We then calculated what the implied fragment length of the sequencing molecule (L_r^i) would be for each isoform i as the distance from the start of the gene to the 3' end of the read (counting only exons included in isoform i). The likelihood of a given read r being derived from a fragment of length L_r^i could then be modeled as

$$L_r^i \sim \mathcal{N}(\mu, \sigma^2),$$

where μ and σ^2 parameterize the mean and variance of the fragment length distribution for the particular sequencing experiment. Conditioning on these parameters, the likelihood of a particular transcript t being a certain isoform can be calculated by the product rule over all the reads r with that transcript's UMI (which we define the set R_t)

$$f\left(\left\{L_r^i, C_{r,i}\right\}_{r \in R_t} \mid I_t = i; \mu, \sigma^2\right) = \prod_{r \in R_t} \mathcal{N}(L_r^i; \mu, \sigma^2) C_{r,i}.$$

The prior probability of a transcript being of a given class was then modeled with a categorical distribution parametrized by the vector π .

$$I_t \sim \text{Categ}(\pi),$$

which allows computation of the posterior probability of a transcript being a particular isoform

$$q_t^i = P\left(I_t = i \mid \left\{L_r^i, C_{r,i}\right\}_{r \in R_t}; \mu, \sigma^2\right) = f\left(\left\{L_r^i, C_{r,i}\right\}_{r \in R_t} \mid I_t = i\right) \pi_i.$$

We then applied expectation–maximization by iteratively computing the above quantity (E-step), and applying the following update rules

$$\mu = \frac{1}{N} \sum_{t \in T} \sum_{i \in S} q_t^i \sum_{r \in R_t} L_r^i$$

$$\sigma^2 = \frac{1}{N} \sum_{t \in T} \sum_{i \in S} q_t^i \sum_{r \in R_t} (L_r^i - \mu)^2$$

and

$$\pi_i = \frac{1}{|T|} \sum_{t \in T} q_t^i,$$

where N is the total number of reads covering CD45, T is the set of all CD45 transcripts (UMIs) and S is the set of the six CD45 isoforms. In our downstream analyses, we then estimated expression of CD45RO and CD45RA (the classification antibody that detects isoforms RA, RAB and RABC) on the same log-transformed

scale as our gene expression data by computing for every cell c with N_c total transcripts and T_c transcripts in CD45

$$\text{expr}_c^{\text{RO}} = \ln \left(1 + \frac{10^4}{N_c} \sum_{t \in T_c} q_t^{\text{RO}} \right)$$

and

$$\text{expr}_c^{\text{RA}} = \ln \left(1 + \frac{10^4}{N_c} \sum_{t \in T_c} \sum_{i=\text{RA,RAB,RABC}} q_i^i \right).$$

Supervised classification of T cell subsets. To label cells, in a fashion consistent with FACS-based literature, we annotated cells based on the expression of commonly used marker genes by thresholding kNN-smoothed ($k=20$) log-normalized expression values as designated in Supplementary Table 6. Conventional T cells were classified by differentiation state as Naive ($CCR7^+CD45RA^+$), CM ($CCR7^+CD45RA^-$), EM ($CCR7^-CD45RA^+$) and TEMRA ($CCR7^-CD45RA^+$). We further distinguished two additional T cell subsets: T_{reg} cells ($FOXP3^+$) and CD4 $^+$ CTLs ($CD4^+NKG7^+$).

Validation of T cell subtype classification using 10x demonstration dataset. BAM files, gene expression and feature barcode matrices for the dataset ‘PBMCs of a Healthy Donor—5’ Gene Expression with a Panel of TotalSeq-C Antibodies’ were downloaded from the 10x Genomics website. CD45 isoforms were quantified from the BAM files using our tool described above. Gene expression and feature barcoding data were normalized in units of log transcripts per 10,000. T cells were selected as cells with a protein expression of CD3 above 7.5, and then a typical scanpy workflow was used to visualize the data by running PCA followed by UMAP. Subpopulations were defined by drawing gates to best separate clusters of cells with different combinations of CD4/CD8 and CD45RA/CCR7 positivity (Extended Data Fig. 4d). In the feature barcoding data, CD8 $^+$ cells had a higher background signal of CD45RA and thus a higher threshold was needed than for CD4 $^+$ cells, whereas in the RNA data a single cutoff could be used for both.

Subclustering of CAR-T populations. We performed subclusterings of CAR-T cells for all eight combinations of CD4/CD8 subtype, IP/D7 timepoint and tis/axi-cel product. Harmony batch correction was used to adjust four samples that had been run without the FACS sorting procedure, using all other samples as a reference. Cells were considered CAR-T if at least a single CAR transcript was observed, or if they shared a TCR sequence with another CAR $^+$ cell. Cells were then processed using the same pipeline outlined above, with the exception that we used fewer (15) PCs and regressed out S and G2M scores. For each of the eight sets, we performed Leiden clustering⁵⁸ to define subpopulations and identified top marker genes with a *t*-test.

Testing for compositional changes. We tested for changes in PBMC population frequencies between responders and nonresponders by running scCODA²² using T cells as a reference. We fit a model using response and product as predictors, and reported cases found to be credible with over 90% inclusion probability (corresponding to a 10% FDR).

When testing overall changes in CAR-T cell populations (Fig. 4b), as a suitable and consistent population to use as a reference is not possible, we used a modified approach. We fit a Dirichlet-multinomial model on the cell counts of each patient with parameters α_R and α_{NR} for responders and nonresponders, respectively. We then calculated a log likelihood ratio statistic between the maximum likelihood of this model (L_1) and that of a null model fixing $\alpha_R = \alpha_{NR}$ (L_0).

$$R = -2\log(L_0/L_1)$$

Finally, we permuted our responder/nonresponder labels 100,000 times, computed a null distribution for R then used this to calculate an empirical P value. We reported a Benjamini–Hochberg FDR-corrected Q value, correcting across the eight categories of CAR-T cells analyzed.

Pseudobulk differential expression analysis. To perform differential expression while controlling for the dependence structure on the cell level introduced by interindividual differences, we applied a pseudobulk method. For each gene, we calculated the total number of UMIs in a given cell population of interest by summing across all cells. Cells from different patients, T cell type (Baseline, Infusion-non-CAR, Infusion-CAR, D7-non-CAR, D7-CAR) and CD4/CD8 subtype were given separate pseudobulk samples, yielding an X by Y matrix of UMI counts. We then analyzed this using a limma⁴⁸ workflow using multilevel modeling to account for multiple pseudobulk samples coming from the same patient. Counts data was voom-transformed, and sample dependency correlations were computed using the patient ID as a blocking variable. The voom transform was then recomputed using a model with the blocking structure. The limma model

was then fitted using gender as a covariate, and contrasts of interest were compared between populations of interest.

IP cell type identification. To identify common cell populations across different types of CAR-T IPs, we reanalyzed just the cells from the IP samples. We used the same workflow as above, with the difference that we performed Harmony batch correction using the patient ID as a batch variable. This removes the (likely biological) differences between the products, but enabled us to identify common populations between the two, more importantly isolating T_{reg} cells in tis-a-cel products.

Independent T_{reg} validation. We downloaded scRNA-seq gene expression matrices of previously published axi-cel infusion products¹⁰ from the Gene Expression Omnibus (GEO accession GSE151511). We filtered cells with ≤ 200 genes and $\geq 10\%$ mitochondrial RNA. Data was processed using the pipeline described above, using 25 PCs and harmony batch correction on the sample level to allow identification of common populations.

CAR- T_{reg} validation. Lentiviral production. Human embryonic kidney cells (HEK293T) were purchased from ATCC and expanded in RPMI 1640 media with GlutaMAX and HEPES (Thermo Fisher Scientific, catalog no. 72400-120) with 10% FBS (R10). Constructs were synthesized and then cloned into a third-generation lentiviral backbone (GenScript). Replication deficient lentivirus was produced by transfecting plasmids into HEK293T cells. Supernatant was collected at 24 and 48 h after transfection. Virus was filtered and then concentrated by ultracentrifugation followed by storage at -80°C .

Bulk T cell isolation and CAR production. Anonymized human healthy donor leukapheresis products were purchased from the Massachusetts General Hospital (MGH) blood bank using an Institutional Review Board-approved protocol. CD3 $^+$ T cells were isolated using a T cell rosette-sep isolation kit (STEMCELL Technologies, catalog no. 15061) and then activated using CD3/CD28 Dynabeads at a 3:1 bead:T cell ratio (Life Technologies, catalog no. 40203D) in R10 with penicillin/streptomycin (Thermo Fisher Scientific, catalog no. 15140122), and 20 IU ml $^{-1}$ recombinant human interleukin (IL)-2 (Peprotech, catalog no. 200-02). CARs were transduced with lentivirus at a multiplicity of infection of five on day 1 and expanded with media doubling and IL-2 replacement every 2–3 days. After 1 week the CARs underwent magnetic debeading, followed by another week of expansion.

T_{reg} isolation and CAR production. CD4 $^+$ T cells were isolated from the autologous donor leukopak (relative to CD3 $^+$ cells) using the Rosette-sep Human CD4 $^+$ T cell negative selection isolation kit with a Ficoll gradient (STEMCELL Technologies, catalog no. 15062). Isolated CD4 $^+$ cells were then enriched for CD25 using CD25-PE antibody staining (BD Bioscience 2A3) and subsequent anti-PE bead selection (Miltenyi Biotec, catalog no. 130-048-801). The resultant two populations (CD4 $^+$ CD25 $^{\text{high}}$, and CD4 $^+$ CD25 $^{\text{low}}$) were then stained with CD4 (BV510 BD Biosciences, catalog no. SK3 562970) used at a dilution of 1 in 20, CD8 (APC-H7 BD Biosciences, catalog no. SK1 560273) used at a dilution of 1:40, CD127 (BV 711 BD Biosciences, catalog no. HIL-7R-M21 561028) used at a dilution of 1 in 20 and 4,6-diamidino-2-phenylindole (DAPI) and sorted on a BD FACSAria for the following populations DAPI-CD4 $^+$ CD8 $^-$ CD25 $^{\text{high127-}}$ (T_{reg} cells) and DAPI-CD4 $^+$,CD8 $^-,$ CD25 $^-$ (Control CD4s).

T_{reg} cells, CD4-control and bulk-CD3 cells were activated with anti-CD3/anti-CD28 human T_{reg} expander beads (Thermo Fisher Scientific 1129D) in CTS OpTmizer T cell expansion Serum Free Media (Thermo Fisher Scientific, catalog no. A1048501) with 2% human serum (Access Cell Culture LLC), 1× GlutaMAX (Thermo Fisher Scientific), 100 U ml $^{-1}$ penicillin-streptomycin and recombinant human IL-2 (300 IU ml $^{-1}$ for T_{reg} cells and 20 IU ml $^{-1}$ for CD4-control). At 1 day after sorting, T cells were transduced at a multiplicity of infection of five with lentivirus. After 1 week, the CARs underwent magnetic debeading, followed by another week of expansion. Transduction efficiency was assessed on day 12–14 after transduction, and nontransduced control cells (T_{reg} cells, CD4-control or bulk-CD3) were added to normalize transduction efficiency across the conditions.

FOXP3 staining. Before activation, samples were drawn from the CD4 $^+$ CD25 $^{\text{high127-}}$ (T_{reg} cells), CD4 $^+$ CD25 $^-$ (Control CD4s) and CD3 $^+$ (Bulk-CD3) groups and stained for FOXP3 (APC Invitrogen PCH101 17-4776-42) using the intracellular staining kit (eBioscience 00-5523-00) used at dilution 1 in 20.

JeKo-1 lymphoma model. NSG (NOD.Cg-PrkdcscidIl2rgtm1Wjl/SzJ) mice were purchased from the Jackson Laboratory and bred in pathogen-free conditions at the MGH Center for Cancer Research and all care and conducted experiments were carried out with protocols approved by the MGH Institutional Animal Care and Use Committee. Animals were housed at temperatures of 21.1–24.5 °C, 30–70% humidity and 12 h:12 h light:dark cycles. On day −7, 6-week-old female NSG mice were engrafted intravenously with 10^6 JeKo-1-click beetle green luciferase (CBG) lymphoma cells (ATCC). On day 0, a total of 1×10^6 fresh CAR-T cells were injected intravenously at the ratios of bulk-CD3, CD4-control and T_{reg} cells as

indicated. Mice were imaged biweekly using p-Luciferin (Fisher Scientific) in an Ami HT (Spectral Instruments Imaging). Images were analyzed using Aura v. 4.0.0 (Spectral Instruments Imaging) software.

At the time of euthanasia, spleens were collected and sectioned. One section was fixed in 10% neutral buffered formalin and the remainder was pulverized mechanically and filtered. Cells were stained for CD3 and analyzed via flow cytometry. All non-FACS sorting flow cytometry was performed on a BD Fortessa X20 utilizing FACSDiva software v.8.0.1.

Formalin-fixed tissue was transferred to 70% ethanol and underwent human CD3 (BD Bioscience UCHT1) staining at the MGH histopathology core. Scale bars were added utilizing Fiji ImageJ (continuously updated, open source, downloaded 2020).

All flow cytometry was analyzed utilizing Flowjo v.10.8.1. Validation analyses for *in vitro* and *in vivo* experiments utilized GraphPad Prism v.9.0 software.

The swimmer plot was generated in RStudio (v.2021.09.1) using the package `swimplot` (v.1.2.0).

Data visualization. All boxplots presented here show the median, interquartile range, and minima and maxima of underlying samples. Overlaid dotplots show individual samples.

Reporting summary. Further information on research design is available in the Nature Research Reporting Summary linked to this article.

Data availability

Gene expression matrices from the scRNA data have been deposited with the Gene Expression Omnibus (GEO accession [GSE197268](#)). Raw sequencing data is available on the database of Genotypes and Phenotypes ([phs002922.v1.p1](#)). Data from a previous study of axi-cel infusion products is available on GEO at [GSE15151](#).

Code availability

Code for our method for measurement of CD45 isoforms is publicly accessible on GitHub at [https://github.com/getzlab/10x-cd45-isoform-quantification](#). Other code supporting the analyses performed in this paper is available at [https://github.com/getzlab/Haradhvala_et_al_2022](#).

References

49. Cheson, B. D. et al. Revised response criteria for malignant lymphoma. *J. Clin. Oncol.* **25**, 579–586 (2007).
50. Tirkes, T. et al. Response criteria in oncologic imaging: review of traditional and new criteria. *Radiographics* **33**, 1323–1341 (2013).
51. Abramson, J. S. et al. Lisocabtagene maraleucel for patients with relapsed or refractory large B-cell lymphomas (TRANSCEND NHL 001): a multicentre seamless design study. *Lancet* **396**, 839–852 (2020).
52. June, C. H., Levine, B. L., Porter, D. L., Kalos, M. D. & Milone, M. C. Use of chimeric antigen receptor-modified t cells to treat cancer. European Patent EP3214091B1 (2017).
53. Kochenderfer, J. N. et al. Construction and preclinical evaluation of an anti-CD19 chimeric antigen receptor. *J. Immunother.* **32**, 689–702 (2009).
54. Wolf, F. A., Angerer, P. & Theis, F. J. SCANPY: large-scale single-cell gene expression data analysis. *Genome Biol.* **19**, 15 (2018).
55. Wolock, S. L., Lopez, R. & Klein, A. M. Scrublet: computational identification of cell doublets in single-cell transcriptomic data. *Cell Syst.* **8**, 281–291.e9 (2019).
56. Ilya, K. N. et al. Fast sensitive and accurate integration of single-cell data with Harmony. *Nat. Methods.* **16**, 1289–1296 (2019).
57. Pachter, L. Models for transcript quantification from RNA-Seq. Preprint at <https://arxiv.org/abs/1104.3889> (2011).
58. Traag, V. A., Waltman, L. & van Eck, N. J. From Louvain to Leiden: guaranteeing well-connected communities. *Sci. Rep.* **9**, 5233 (2019).

Acknowledgements

We thank E. Berg, M. O'Reilly and the rest of the Broad Institute Patterns team for their contributions to the figure design. This work was partially supported by the Broad/IBM Cancer Resistance Research Project (principal investigators (PIs): G.G., L.P.) and by National Institutes of Health (NIH) R01CA252940 (PIs: M.V.M. and G.G.). A special thank you to S. Arrom and D. Oran for their thoughtful donation that helped to support a portion of this work. N.J.H. was partially funded by the Landry Cancer Biology Consortium fellowship. S.L. is supported by the National Cancer Institute Research Specialist Award (R50CA251956). R.C.L. is supported by NIH T32 AI007529. BioRender.com was utilized for Extended Data Fig. 6c.

Author contributions

N.J.H., M.B.L., K.M., S.H.G., R.C.L., C.J.W., G.G. and M.V.M. conceived and designed the study. M.B.L., K.M., S.H.G., C.J. and J.F. collected patient samples and clinical data. M.B.L., K.M., K.M.E.G., K.K., S.H.G. and R.C.L. processed patient samples. S.L., J.S. and K.J.L. performed the sequencing. N.J.H. analyzed the data. N.J.H., M.B.L., K.M., S.H.G., R.C.L., N.Y., K.R., F.U., C.L., B.P.D., L.P., C.J.W., G.G. and M.V.M. interpreted the data. M.B.L., H.S., M.C.K. and M.J. performed *in vitro* and *in vivo* experiments. R.A.J., K.S., M.J.F. and B.P.D. participated in project administration. C.J.W., G.G. and M.V.M. supervised the work. N.J.H., M.B.L., K.M., S.H.G., C.J.W., G.G. and M.V.M. wrote the manuscript. N.J.H., M.B.L., K.M., S.H.G., R.C.L., N.Y., K.M.E.G., S.L., K.R., F.U., C.J.W., G.G. and M.V.M. revised the manuscript.

Competing interests

N.J.H. is a consultant for MorphoSys. C.J.W. holds equity in BioNTech Inc. and receives research funding from Pharmacyclics. S.H.G. holds patents related to adoptive cell therapies, held by University College London and Novalgen Limited. S.H.G. provides consultancy to Novalgen Ltd. G.G. receives research funds from IBM and Pharmacyclics, and is an inventor on patent applications related to MSMuTect, MSMuSig, MSIDetect, POLYSOLVER and SignatureAnalyzer-GPU. G.G. is a founder, consultant and holds privately held equity in Scorpion Therapeutics. M.V.M., M.B.L. and R.C.L. are inventors on patents related to adoptive cell therapies, held by MGH. M.V.M. is also an inventor on patents related to CAR-T cell therapies held by the University of Pennsylvania (some licensed to Novartis). M.V.M. is on the Board of Directors of 2SeventyBio, and holds equity in TCR2, Century Therapeutics, Oncternal and Neximmune, and has served as a consultant for multiple companies involved in cell therapies. The other authors declare no competing interests.

Additional information

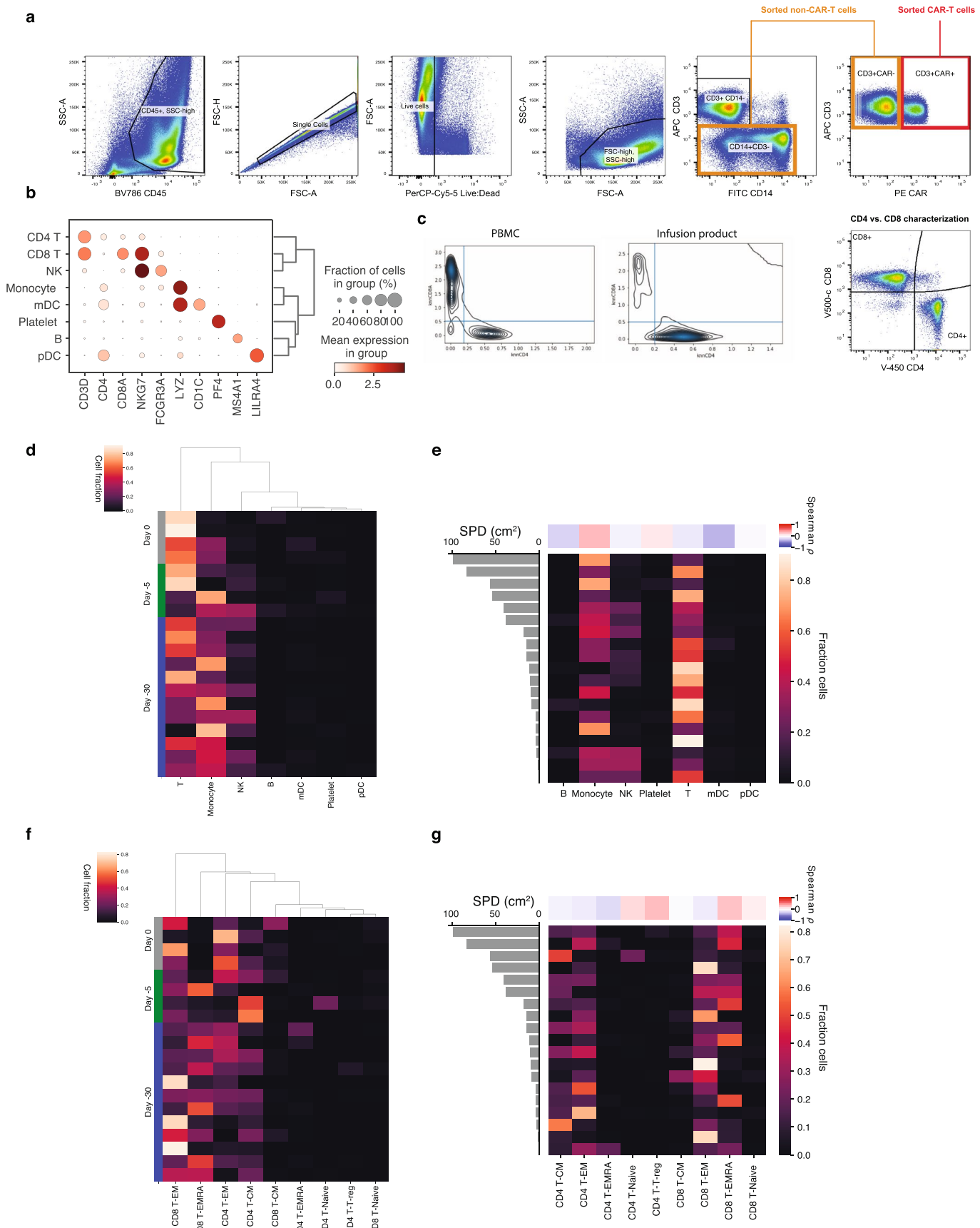
Extended data is available for this paper at <https://doi.org/10.1038/s41591-022-01959-0>.

Supplementary information The online version contains supplementary material available at <https://doi.org/10.1038/s41591-022-01959-0>.

Correspondence and requests for materials should be addressed to Catherine J. Wu, Gad Getz or Marcela V. Maus.

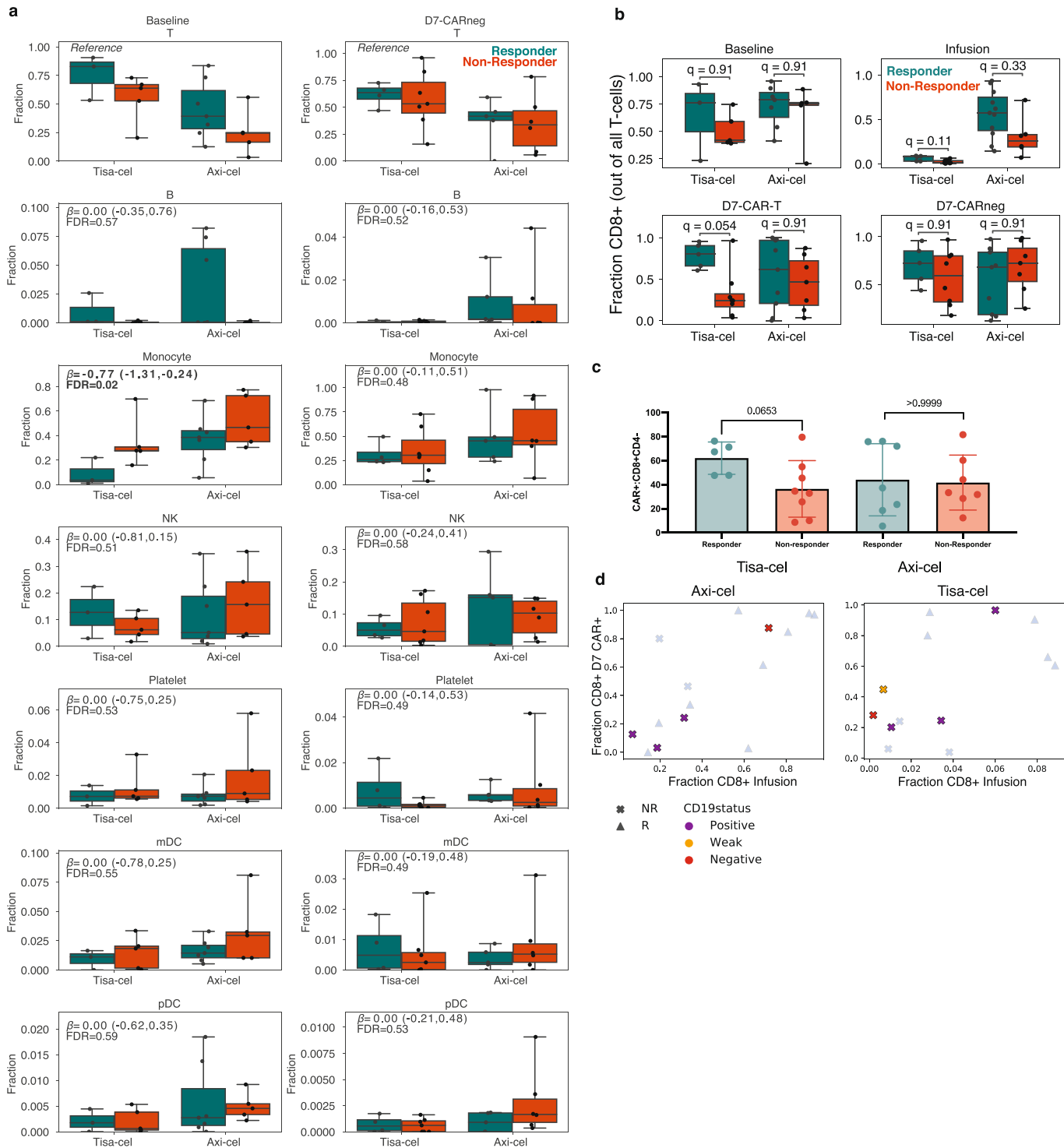
Peer review information *Nature Medicine* thanks Sattva Neelapu and the other, anonymous, reviewer(s) for their contribution to the peer review of this work. Primary Handling Editors: Sahelin Sadanand and Joao Monteiro, in collaboration with the *Nature Medicine* team.

Reprints and permissions information is available at www.nature.com/reprints.



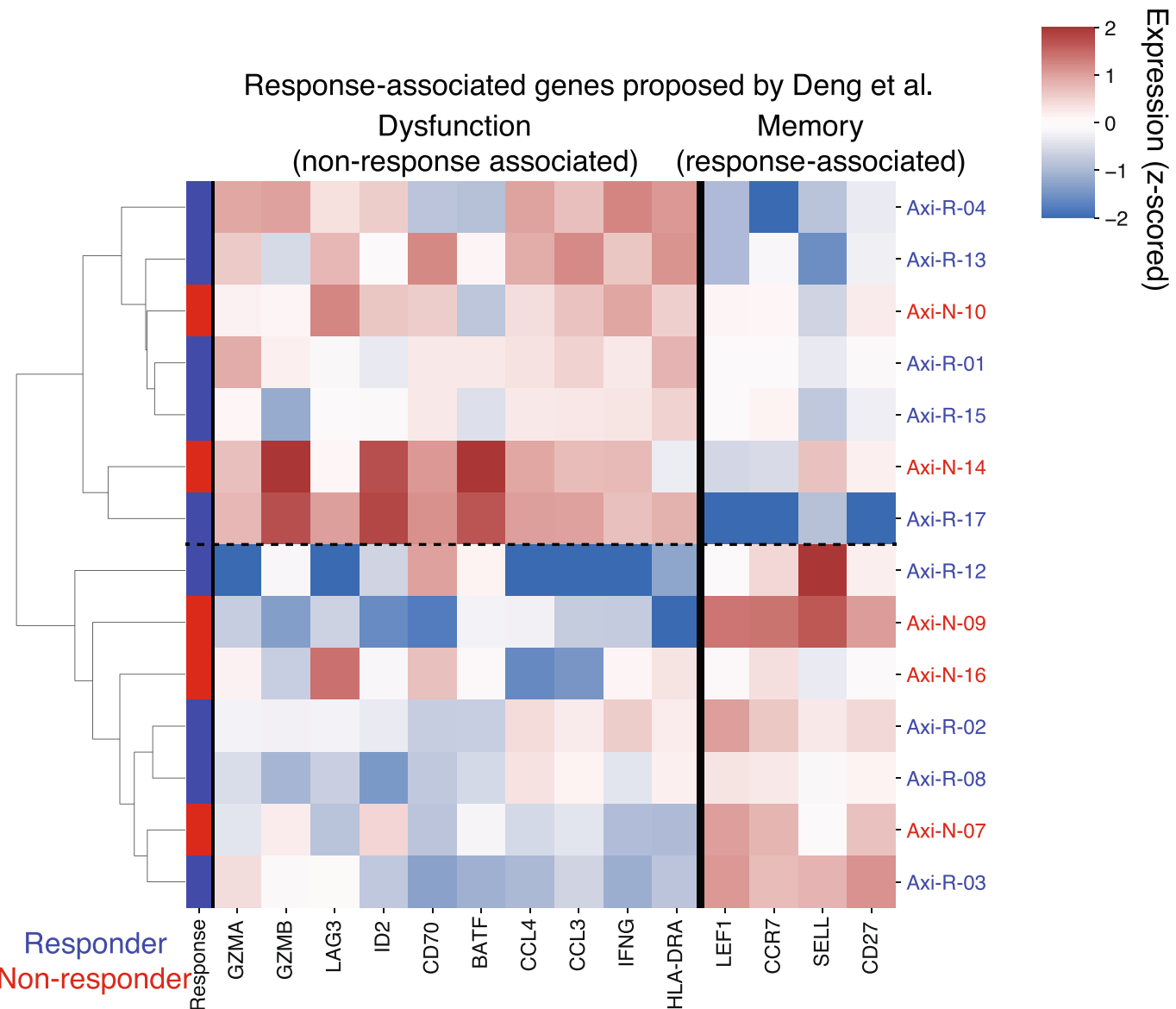
Extended Data Fig. 1 | See next page for caption.

Extended Data Fig. 1 | Single-cell isolation and classification. **a**, Live CD14-CD3+CAR+ cells were isolated as CAR-T cells while CD3+CAR- cells were combined with CD14+CD3- cells as non-CAR-T cells for subsequent scRNA-seq workflows. **b**, Selected marker genes for PBMC cell population identification in scRNA-seq data. **c**, Kernel density estimate plots of knn-smoothed ($k=100$) CD4 and CD8A expression across cells at day 7 and in the IP. Lines are drawn for thresholds used for classification. **d**, Fractions of cells of each coarse cell type for every baseline sample sorted by timepoint of sampling, as well as **e**, baseline tumor volume, measured by SPD (cm^2). The same shown for **f,g** fine-grained T cell subsets.

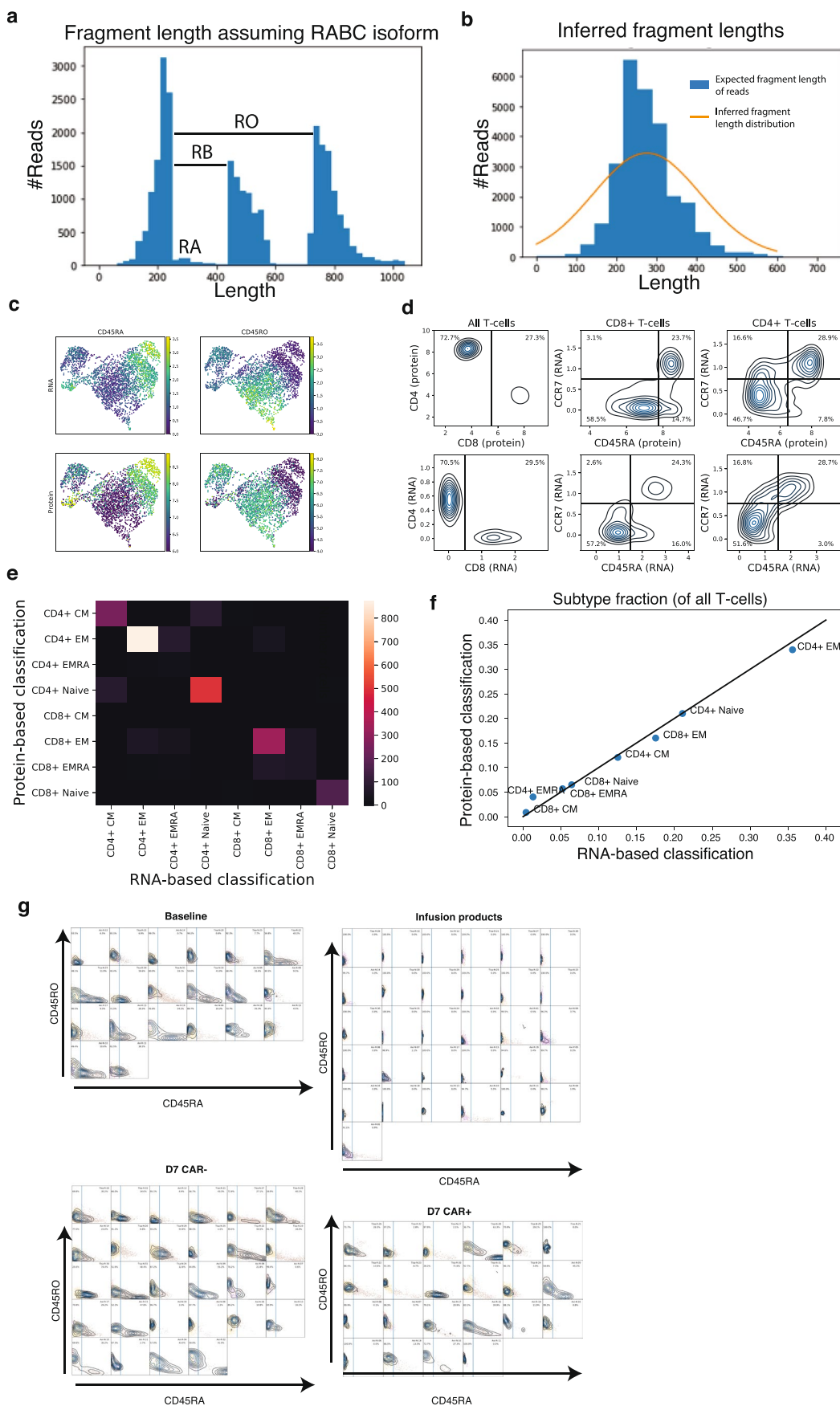


Extended Data Fig. 2 | PBMC cell composition differences between responders and non-responders pre- and post-infusion. **a**, Boxplots of the cell type frequencies for each cell type stratified by product and response. The final cell type coefficient (with its posterior 95% high density interval) and FDR value (one minus the inclusion probability) estimated by scCODA are shown. Boxes show the median, interquartile range, and maximum/minimum values. n=20 and n=22 biologically independent samples are shown for baseline and D7-CAR-negative samples, respectively. **b**, Fraction of cells which were CD8+CD4- at baseline, in IPs, and at day 7 in CAR+ and CAR- populations. Boxes show the median, interquartile range, and maximum/minimum values. n=20 baseline, n=30 infusion, n=29 day 7 CAR-negative, and n=29 day 7 CAR-positive independent samples are shown from 31 patients.

c, Flow-cytometric measurements for the mean fraction of CAR positive cells which were CD8+CD4- at day 7 for n=27 biologically independent samples. Error bars represent standard deviation. P-values represent two-tailed Mann -Whitney U tests. **d**, Changes in CD8+ frequencies between IP and day 7 CAR-T cells as shown in Fig. 3b, colored by CD19 status of relapse. Samples with no relapse, or relapse without a biopsy, are grayed out.

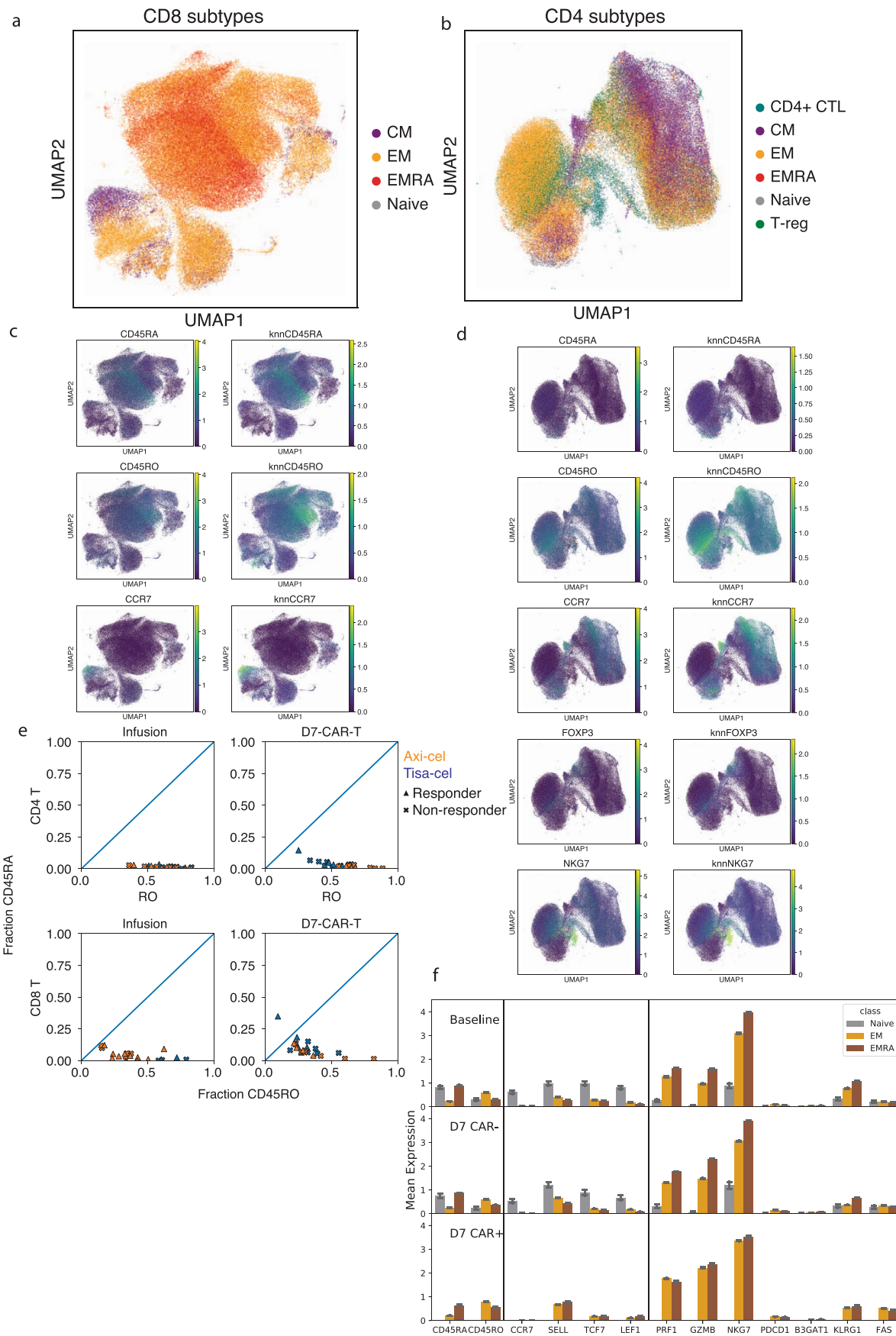


Extended Data Fig. 3 | Expression of previously proposed axi-cel response genes. Pseudobulk expression (z-scored log transcripts per million) of CD8+CAR-T axi-cel IP cells for genes proposed to be response-associated by Deng et al. Fisher Exact test for association between response and denoted two clusters driven by putative memory- and dysfunction-associated genes is $p=1$.



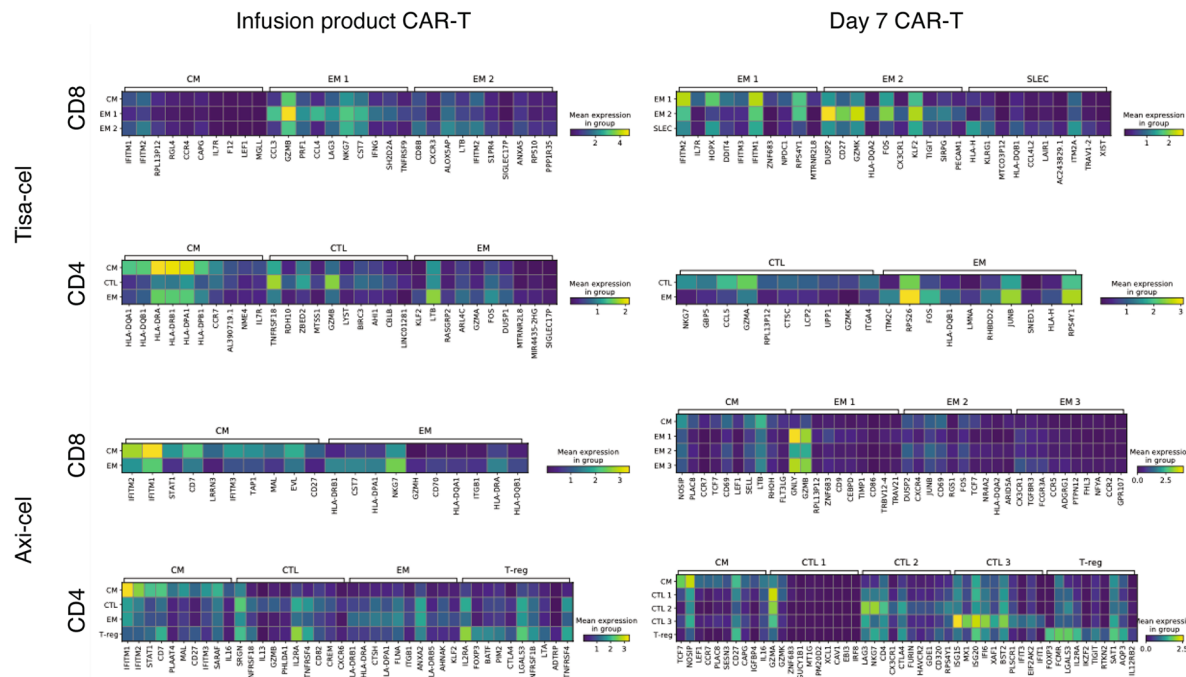
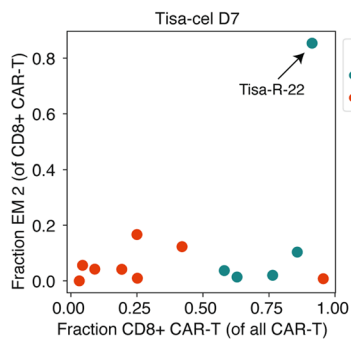
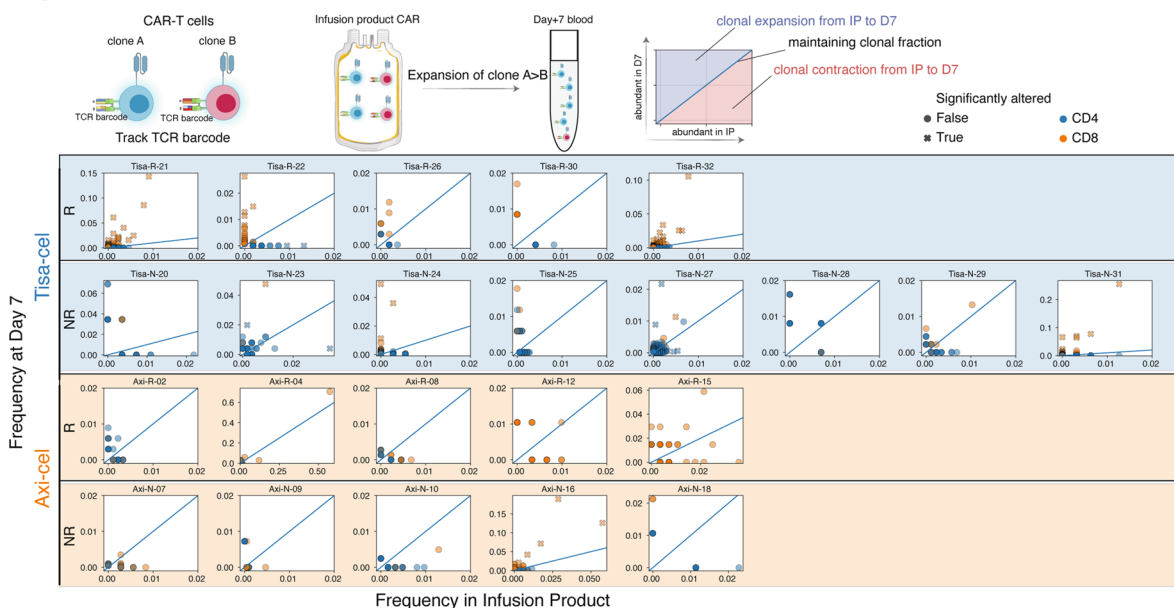
Extended Data Fig. 4 | See next page for caption.

Extended Data Fig. 4 | Detection of CD45 isoforms and T cell subset classification in 5' RNA-sequencing data. **a**, Illustration of signal used by CD45 isoform detection model. For each read in an illustrative sample, a histogram of the fragment length assuming no splicing (RABC isoform) is shown. The distribution of reads beyond exon 3 become shifted if they come from an isoform lacking an upstream exon. **b**, A histogram of the expected fragment length after inference of each read is shown for the same sample in blue. The gaussian distribution modeling fragment lengths inferred by EM is plotted in orange. **c**, U-MAP representation of T cells in 10x healthy PBMC demonstration dataset with both RNA-sequencing and feature-barcoding measurements. Dataset is colored by CD45RA and CD45RO expression measured by RNA (top, with $k=20$ knn smoothing as applied in the paper) and feature barcoding (bottom). **d**, Kernel density estimate plots sorting plots of cells into different memory subsets. Black lines represent cutoff used for gating. **e**, Confusion matrix showing concordance of cell classification by protein-based and RNA-based approaches. **f**, Scatterplot showing similarity of cell fraction measurements using either the RNA-based (x-axis) or protein-based (y-axis) measurements. **g**, Kernel density estimate distributions of knn-smoothed ($k=20$) CD45RA (x-axis) and CD45RO (y-axis) expression measurements in our dataset for Baseline T cells, Infusion products, day 7 CAR- cells and day 7 CAR+ cells. A plot is shown for each sample, and the CD45RA cutoff used for classification is drawn with a blue line. All plots share x and y axis scales.

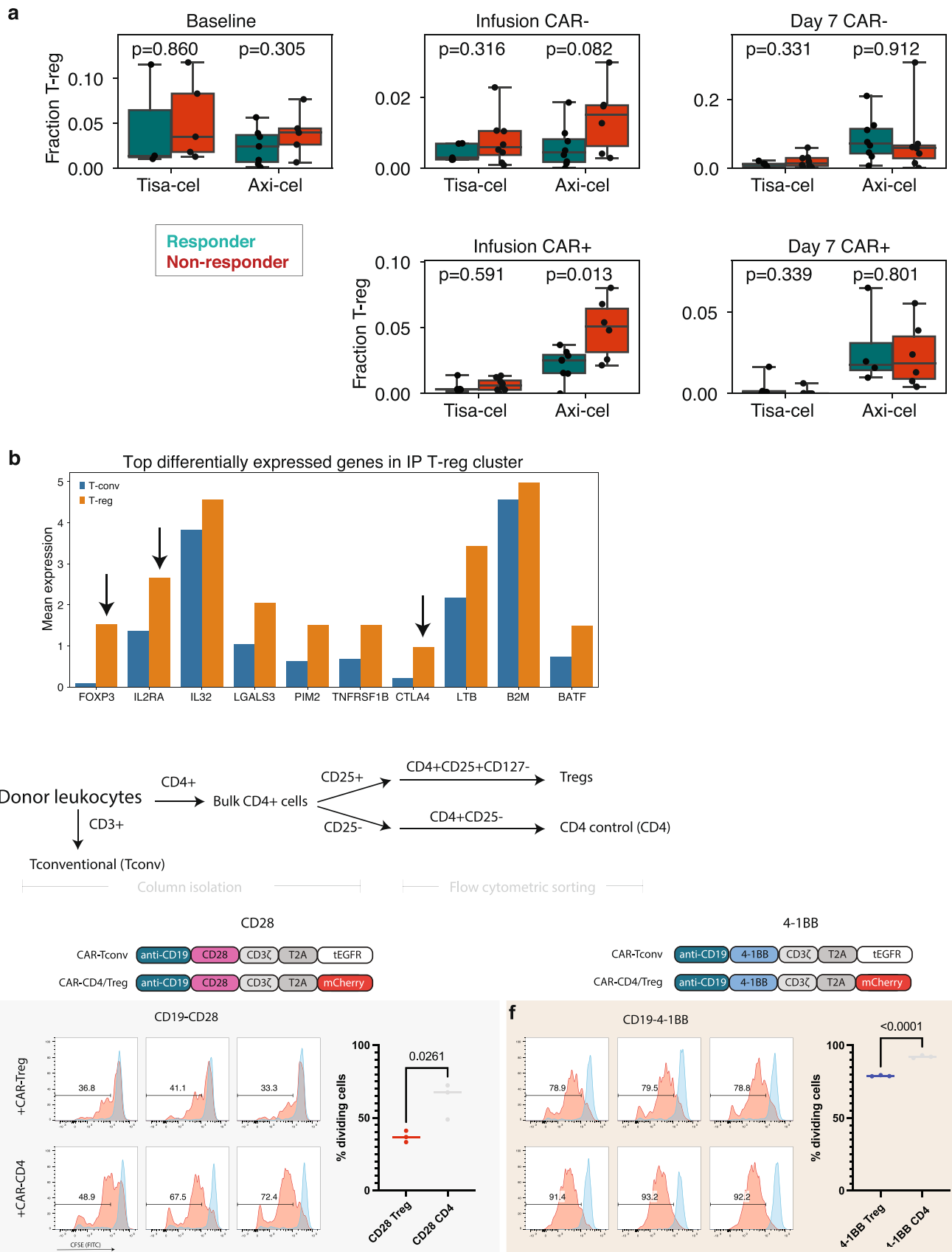


Extended Data Fig. 5 | See next page for caption.

Extended Data Fig. 5 | Classification of T cell subtypes. UMAP representations of all **a**, CD8 and **b**, CD4 T cells colored by their subtype assignment. Expression of marker genes used for subtype assignment for **c**, CD8 and **d**, CD4 cells. For each a kNN-smoothed ($k=25$) estimate is shown (right) alongside the raw measurements (left). **e**, Estimated fractions of CD45 isoforms that are RO (x-axis) or RA (y-axis) in CAR-T cells from infusion products and at day 7. **f**, Mean expression of genes related to differentiation state averaged across Naive, EM and TEMRA cells for Baseline T cells, day 7 CAR-T cells. Naive cells for day 7 CAR+ were omitted as they were not seen in quantities that could be analyzed. Error bars represent 95% confidence intervals derived from bootstrapping cells for 1000 iterations. Shown are $n=20,361$ baseline (12,799 EM, 7,108 TEMRA, and 454 Naive) cells from 20 individuals, as well as $n=46,750$ day 7 CAR-negative (24,436 EM, 22,064 TEMRA, and 250 Naive), and $n=10,010$ day 7 CAR-positive (8,712 EM and 1,298 TEMRA) T cells from 29 individuals.

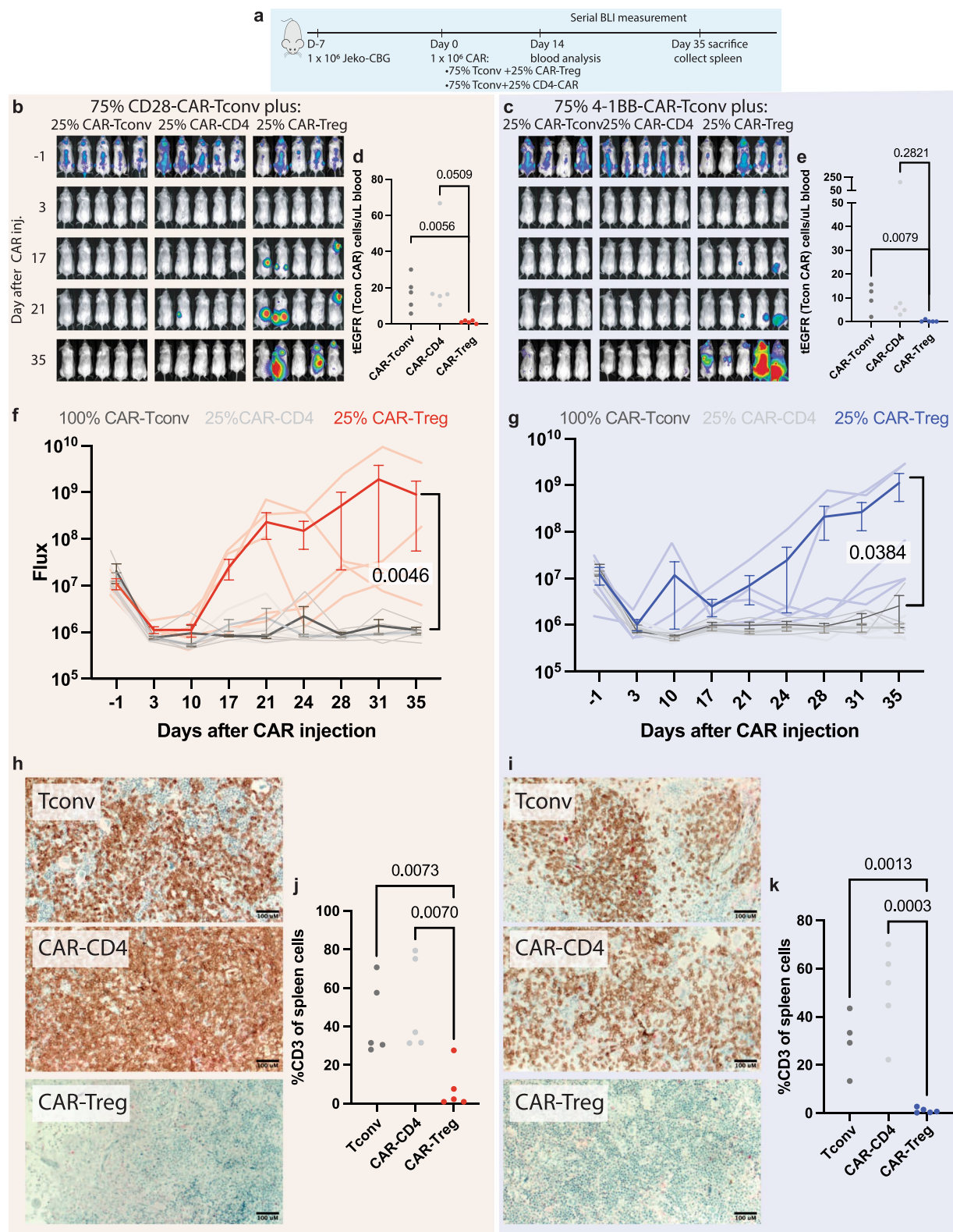
a**b****c****Extended Data Fig. 6 | See next page for caption.**

Extended Data Fig. 6 | CAR-T subclusters and clonal dynamics. **a**, Top differentially expressed genes in each CAR-T subcluster, as determined by a t-test. The expression is shown for the top 10 marker genes of each cluster displayed in Fig. 4a. **b**, Demonstration of unique tis-a-cel responder with CD8+ cells in cluster EM 2. Shown is a scatterplot of the fraction of CD8+ cells in cluster EM 2 (y-axis) vs the fraction of all CAR-T cells that are CD8+ (x-axis). **c**, For each patient with at least 25T cells in both the IP and at day 7, individual TCR clones are plotted by their frequency in the IP (x-axis) and at day 7 (y-axis). Clones are colored by whether they are CD8+ or CD4+, and denoted with an 'x' if the two timepoint frequencies are significantly different by a two-tailed fisher exact test $p < 0.05$.



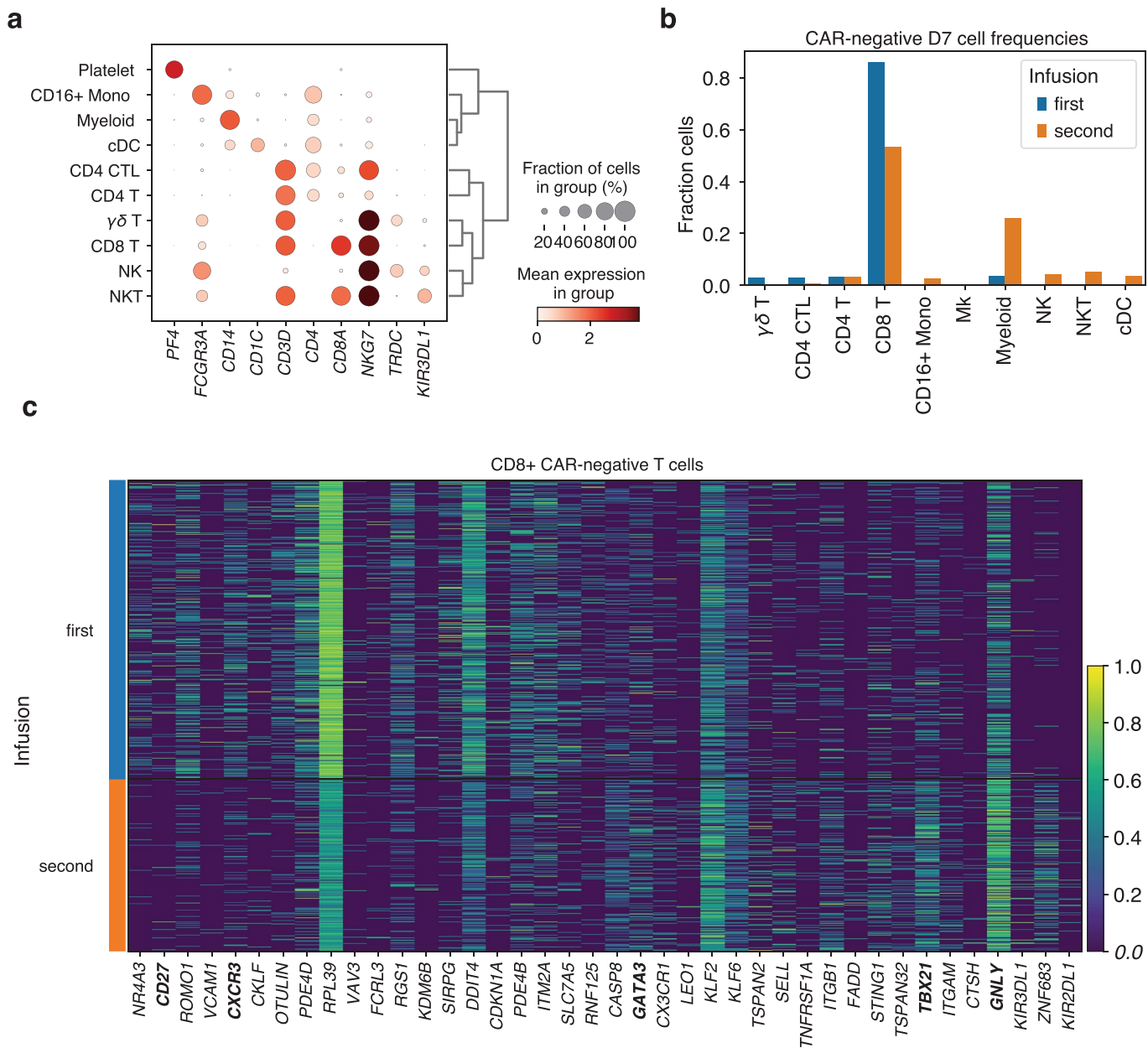
Extended Data Fig. 7 | See next page for caption.

Extended Data Fig. 7 | Regulatory T cells characteristics and *in vitro* suppression. **a**, The fraction of T cells that are T-reg in samples of each timepoint, separated by CAR+ and CAR- cells. Only samples with at least 100 T cells of the relevant type are included in the analysis. A total of n=20 baseline, n=27 Infusion CAR-negative, n=27 Infusion CAR-positive, n=28 day 7 CAR-negative and n=22 day 7 CAR-positive biologically independent samples are shown. P-values denote a two-tailed t-test without correction for multiple hypotheses. Boxes show the median, interquartile range, and maximum/minimum values. **b**, Average expression in IP T-reg (orange) and all other T cells (T-conv, blue) of the top 10 differentially expressed genes comparing T-reg and T-conv in IP cells. Genes classically associated with T-reg function are highlighted with arrows. **c**, Schematic for T-reg and CD4 control population isolation from healthy donor PBMC. **d**, CAR constructs used to identify CAR-T_{reg}/CD4-CAR cells from CAR-Tconv. **e,f**, CFSE staining of CAR-Tconv cells co-cultured with either 25% CAR-T_{reg}s or CD4-CAR control cells and stimulated at a 1:1 ratio with Jeko tumor targets at 72 hours. Dividing cells (red) are identified relative to unstimulated condition (blue). Each histogram represents an individual replicate, summarized in the plot on the right for all n=3 technical replicates per construct over 1 independent experiment. P-value represents two-tailed unpaired t-test.

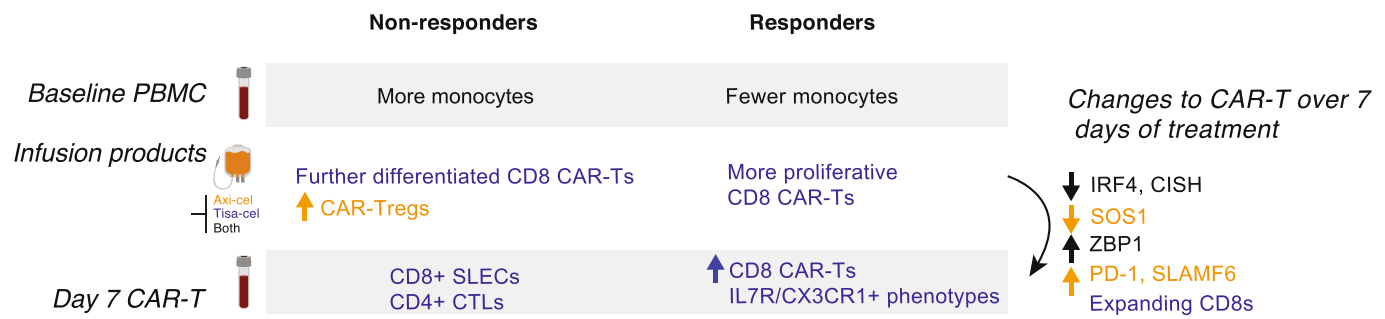


Extended Data Fig. 8 | See next page for caption.

Extended Data Fig. 8 | Mediation of relapse by CAR-T_{reg}s at 25% via *in vivo* validation experiments. **a**, NSG mice were injected with 1×10^6 Jeko-CBG lymphoma cells on day -7. On day 0 mice were injected with 1×10^6 CAR-T cells representing 100% CAR-T convs or 75% CAR-Tconv with either 25% CAR-T_{reg}s or 25% CD4-CAR-T control cells. Experiment performed with CD19-CD28 (left) or CD19-4-1BB (right) constructs. **b, c** Time course tumor radiance (photons/sec/cm²/sr). **d, e** Flow cytometric quantification of CAR-Tconv day 14 after CAR injection for n=15 biologically independent animals per construct examined over 1 independent experiment. P-value represents two-tailed unpaired t-test. **f, g** Time course flux (photons/s). Mean \pm SEM overlaid on individual subject curves for n=14 biologically independent animals per construct examined over 1 independent experiment. P-value represents the result of two-way ANOVA. **h, i** Representative immunohistochemical staining for human CD3 in the spleen. **j, k** Flow cytometric quantification of CD3 cells from the spleens of the indicated conditions for n=15 (CD28) and n=14 (4-1BB) biologically independent animals examined over 1 independent experiment. P-value represents two-tailed unpaired t-test.



Extended Data Fig. 9 | Changes in PBMC populations in patient treated with second infusion of tisa-cel. **a**, Expression of marker genes for PBMC cell type classification. **b**, Fractions of day 7 CAR-negative cells falling into each cell type cluster, stratified by first and second infusion. **c**, Top 20 genes differentially increased and decreased (by Mann-Whitney U test) comparing CD8+CAR-negative T cells between the first and second treatments at day 7. Plotted expression values for each gene are log transcripts-per-10,000 translated and scaled to a range of [0,1] based on the minimum and maximum observed values.



Extended Data Fig. 10 | Summary of cellular and transcriptomic changes associated with clinical outcome and timepoint. Graphic depicting the cellular associations of response and temporal changes identified in this study.

Reporting Summary

Nature Portfolio wishes to improve the reproducibility of the work that we publish. This form provides structure for consistency and transparency in reporting. For further information on Nature Portfolio policies, see our [Editorial Policies](#) and the [Editorial Policy Checklist](#).

Statistics

For all statistical analyses, confirm that the following items are present in the figure legend, table legend, main text, or Methods section.

n/a Confirmed

- The exact sample size (n) for each experimental group/condition, given as a discrete number and unit of measurement
- A statement on whether measurements were taken from distinct samples or whether the same sample was measured repeatedly
- The statistical test(s) used AND whether they are one- or two-sided
 - Only common tests should be described solely by name; describe more complex techniques in the Methods section.*
- A description of all covariates tested
- A description of any assumptions or corrections, such as tests of normality and adjustment for multiple comparisons
- A full description of the statistical parameters including central tendency (e.g. means) or other basic estimates (e.g. regression coefficient) AND variation (e.g. standard deviation) or associated estimates of uncertainty (e.g. confidence intervals)
- For null hypothesis testing, the test statistic (e.g. F , t , r) with confidence intervals, effect sizes, degrees of freedom and P value noted
 - Give P values as exact values whenever suitable.*
- For Bayesian analysis, information on the choice of priors and Markov chain Monte Carlo settings
- For hierarchical and complex designs, identification of the appropriate level for tests and full reporting of outcomes
- Estimates of effect sizes (e.g. Cohen's d , Pearson's r), indicating how they were calculated

Our web collection on [statistics for biologists](#) contains articles on many of the points above.

Software and code

Policy information about [availability of computer code](#)

Data collection	Flow cytometry was collected using BD FACSDiva software v8.0.1.
Data analysis	Raw gene expression and TCR-sequencing data was processed using cellranger v6.0.1. Souporcell v2020.7 was used to demultiplex pooled samples. Ambient contamination was filtered using cellbender v0.2.0. Standard single-cell analyses were performed using scanpy v1.8.1. Doublets were filtered using scrublet v0.2.1. In vivo images were analyzed using Aura software v4.0.0. Validation analyses for in vitro and in vivo experiments utilized GraphPad Prism 9.0 software. Flow cytometry data with analyzed using Flowjo v10.8.1. The swimmers plot was generating using RStudio v2021.09.1 and the package swimplot v1.2.0. Our tool for CD45 isoform quantification is available at https://github.com/getzlab/10x-cd45-isoform-quantification . Other custom code used in this work is available at https://github.com/getzlab/Haradhvala_et_al_2022 .

For manuscripts utilizing custom algorithms or software that are central to the research but not yet described in published literature, software must be made available to editors and reviewers. We strongly encourage code deposition in a community repository (e.g. GitHub). See the Nature Portfolio [guidelines for submitting code & software](#) for further information.

Data

Policy information about [availability of data](#)

All manuscripts must include a [data availability statement](#). This statement should provide the following information, where applicable:

- Accession codes, unique identifiers, or web links for publicly available datasets
- A description of any restrictions on data availability
- For clinical datasets or third party data, please ensure that the statement adheres to our [policy](#)

Gene expression matrices from the scRNA data have been deposited to the Gene Expression Omnibus (GEO accession GSE197268). Raw sequencing data have been deposited to the database of Genotypes and Phenotypes (phs002922.v1.p1). Data from a prior study of axi-cel infusion products is available at GSE151511.

Field-specific reporting

Please select the one below that is the best fit for your research. If you are not sure, read the appropriate sections before making your selection.

Life sciences Behavioural & social sciences Ecological, evolutionary & environmental sciences

For a reference copy of the document with all sections, see nature.com/documents/nr-reporting-summary-flat.pdf

Life sciences study design

All studies must disclose on these points even when the disclosure is negative.

Sample size	No statistical methods were used to pre-determine sample size. The study was designed to make a minimum of 3 patients of each response category for each treatment product.
Data exclusions	No samples were excluded from this study.
Replication	Findings in scRNA data were, when possible, explored in other publicly available datasets (Deng et al. 2020) or supported with in vitro and in vivo experiments. Experiments were performed a single time with multiple technical replicates as noted in the figure legends.
Randomization	No randomization was performed for patient studies as this was an observational study of response. Mice were randomized prior to CAR-T treatment to ensure equivalent tumor burden among groups.
Blinding	Blinding was not possible for the analyses of patient data as this study involved data exploration without predetermined knowledge of the cellular features that would be relevant to test. For animal experiments one veterinary technician was in charge of injecting all mice for bioluminescent readings and was blinded to the expected outcomes.

Reporting for specific materials, systems and methods

We require information from authors about some types of materials, experimental systems and methods used in many studies. Here, indicate whether each material, system or method listed is relevant to your study. If you are not sure if a list item applies to your research, read the appropriate section before selecting a response.

Materials & experimental systems

n/a	Involved in the study
<input type="checkbox"/>	<input checked="" type="checkbox"/> Antibodies
<input type="checkbox"/>	<input checked="" type="checkbox"/> Eukaryotic cell lines
<input checked="" type="checkbox"/>	<input type="checkbox"/> Palaeontology and archaeology
<input type="checkbox"/>	<input checked="" type="checkbox"/> Animals and other organisms
<input type="checkbox"/>	<input checked="" type="checkbox"/> Human research participants
<input checked="" type="checkbox"/>	<input type="checkbox"/> Clinical data
<input checked="" type="checkbox"/>	<input type="checkbox"/> Dual use research of concern

Methods

n/a	Involved in the study
<input checked="" type="checkbox"/>	<input type="checkbox"/> ChIP-seq
<input type="checkbox"/>	<input checked="" type="checkbox"/> Flow cytometry
<input checked="" type="checkbox"/>	<input type="checkbox"/> MRI-based neuroimaging

Antibodies

Antibodies used

The following antigens were stained using the indicated antibody clones for flow cytometry analysis CD45 (BV786 BD HI30, 563716). Used at dilution of 1 in 167. CD3 (APC BD Biosciences, SK3, 340661). Used at dilution of 1 in 83.5. CD4 (V450 BD Bioscience SK3, 651850). Used at dilution of 1 in 83.5. CD8 (V500c BD Bioscience SK1, 647458). Used at dilution of 1 in 83.5. CD14 (FITC BD Bioscience MφP9, 347493). Used at dilution of 1 in 83.5. Human CD19 Fc Chimera (carrier free) (PE, BioLegend custom conjugation , 900002598, lot B324342) Used at dilution of 1 in 55.6. CD4 (BV510 BD Biosciences SK3 562970) used at a dilution 1 in 20, CD8 (APC-H7 BD Biosciences SK1 560273) used at dilution 1:40, CD127 (BV711 BD Biosciences HIL-7R-M21 561028) used at dilution of 1 in 20,

FOXP3 (APC Invitrogen PCH101 17-4776-42) used at dilution 1 in 20.

Validation

All antibodies were independently titrated and validated using healthy PBMC followed by Axi-cel and Tisa-cel infusion product prior to use in experiments in this manuscript.

All BD antibodies were provided with a certificate of analysis and were used within their expiry dates.

"This product complies with all BDB release criteria. BD Biosciences San Jose is a registered facility with the US Food and Drug Administration subject to the requirements of 21CFR Part 820 for the manufacture of in vitro diagnostic products. BD Biosciences San Jose also holds the following international standard certifications for Medical Device

--

Quality Management Systems:

ISO 9001:2015, Certificate

FM 32438

ISO 13485:2016, Certificate MDSAP 690529

EN ISO 13485:2016, Certificate MD 605599

Invitrogen antigen statement from manufacturer "This Antibody was verified by Relative expression to ensure that the antibody binds to the antigen stated."

Eukaryotic cell lines

Policy information about [cell lines](#)

Cell line source(s)

JeKo-1 and HEK-293T were acquired from American Type Culture Collection (ATCC).

Authentication

Cell lines were authenticated using STR profiling

Mycoplasma contamination

All cell lines tested negative for mycoplasma contamination.

Commonly misidentified lines
(See [ICLAC](#) register)

No commonly misidentified cell lines were used in the study

Animals and other organisms

Policy information about [studies involving animals; ARRIVE guidelines](#) recommended for reporting animal research

Laboratory animals

NSG (NOD.Cg-PrkdcscidIl2rgtm1Wjl/SzJ) mice were purchased from Jackson Laboratory and bred in pathogen-free conditions at the MGH Center for Cancer Research. 6 week old female NSG mice were engrafted for experiments.

Wild animals

This study did not involve wild animals

Field-collected samples

This study did not involve samples collected from the field

Ethics oversight

Mice were maintained at the MGH Center for Cancer Research and all care and conducted experiments were carried out using protocols approved by the Massachusetts General Hospital Institutional Animal Care and Use Committee.

Note that full information on the approval of the study protocol must also be provided in the manuscript.

Human research participants

Policy information about [studies involving human research participants](#)

Population characteristics

Age, gender, and information about prior treatment for all patients contributing samples for scRNA-seq are detailed in Supplementary Table 1. Healthy donor T-cells were obtained from purchased leukopaks at the MGH blood bank which were obtained from volunteers and are considered non-human subjects research. Demographic information such as age, sex, etc are not available for these volunteers.

Recruitment

Patients with aggressive B-cell lymphoma who were treated with axicabtagene ciloleucel or tisagenlecleucel were selected for inclusion based on having the appropriate diagnosis, sample and cell number availability for the required time points, and attempting to balance the number of responders and non-responders included. Patients were not strictly randomly or prospectively chosen and the number of non-responders in our cohort is artificially inflated for the purposes of our study compared to what is expected based on the performance of the two CAR-T cell products. No compensation was provided for participation. Healthy donors were volunteers from MGH blood bank; considered non-human subjects research.

Ethics oversight

Samples were obtained after written informed consent under IRB-approved protocols at the Dana-Farber/Harvard Center Center (DFHCC #16-206 and 17-561).

Note that full information on the approval of the study protocol must also be provided in the manuscript.

Flow Cytometry

Plots

Confirm that:

- The axis labels state the marker and fluorochrome used (e.g. CD4-FITC).
- The axis scales are clearly visible. Include numbers along axes only for bottom left plot of group (a 'group' is an analysis of identical markers).
- All plots are contour plots with outliers or pseudocolor plots.
- A numerical value for number of cells or percentage (with statistics) is provided.

Methodology

Sample preparation

Tumor cells were cultured as recommended by ATCC. CAR T cells were generated from healthy donors with lentiviral transduction.

Instrument

BD Fortessa-X20

Software

Flow cytometry was collected using BD FACSDiva software v8.0.1 and analyzed using Flowjo v10.8.1

Cell population abundance

Sorted samples were evaluated via scRNAseq as discussed in the study design resulting in additional confirmation of population identities (e.g CAR+ and CD4/CD8 populations)

Gating strategy

Sorted cells were assessed with viability using 7-AAD and gated on single cells. Gate boundaries were established from simultaneous staining of healthy donor PBMC fractions with each sorting batch.

- Tick this box to confirm that a figure exemplifying the gating strategy is provided in the Supplementary Information.